

ON THE REDSHIFT DISTRIBUTION OF GAMMA RAY BURSTS IN THE *Swift* ERA

TRUONG LE¹ AND CHARLES D. DERMER²

E. O. Hulburt Center for Space Research
 Naval Research Laboratory,
 Washington, DC 20375, USA

ApJ, accepted for publication

ABSTRACT

A simple physical model for long-duration gamma ray bursts (GRBs) is used to fit the redshift (z) and the jet opening-angle distributions measured with earlier GRB missions and with *Swift*. The effect of different sensitivities for GRB triggering is sufficient to explain the difference in the z distributions of the pre-*Swift* and *Swift* samples, with mean redshifts of $\langle z \rangle \cong 1.5$ and $\langle z \rangle \cong 2.7$, respectively. Assuming that the emission properties of GRBs do not change with time, we find that the data can only be fitted if the comoving rate-density of GRB sources exhibits positive evolution to $z \gtrsim 3 - 5$. The mean intrinsic beaming factor of GRBs is found to range from $\approx 34 - 42$, with the *Swift* average opening half-angle $\langle \theta_j \rangle \sim 10^\circ$, compared to the pre-*Swift* average of $\langle \theta_j \rangle \sim 7^\circ$. Within the uniform jet model, the GRB luminosity function is $\propto L_*^{-3.25}$, as inferred from our best fit to the opening angle distribution. Because of the unlikely detection of several GRBs with $z \lesssim 0.25$, our analysis indicates that low redshift GRBs represent a different population of GRBs than those detected at higher redshifts. Neglecting possible metallicity effects on GRB host galaxies, we find that ≈ 1 GRB occurs every 600,000 yrs in a local L_* spiral galaxy like the Milky Way. The fraction of high-redshift GRBs is estimated at 8 – 12% and 2.5 – 6% at $z \geq 5$ and $z \geq 7$, respectively, assuming continued positive evolution of the GRB rate density to high redshifts.

Subject headings: gamma-rays: bursts — cosmology: theory

1. INTRODUCTION

Gamma-ray bursts (GRBs) are brief flashes of γ rays occurring at an average rate of a few per day throughout the universe. The ultimate energy source of a GRB is believed to be associated with a catastrophic event associated with black-hole formation (Mészáros & Rees 1997). This event takes place through the collapse of the core of a massive star in the case of long-duration GRBs, and due to merger or accretion-induced collapse events for the short-hard class of GRBs. For the class of long-duration GRBs, which is the only type considered in this paper, liberation of energy from the GRB source is thought to result in a very high temperature, baryon-dilute fireball that expands to reach highly relativistic speeds and form a collimated outflow. Dissipation of the directed kinetic energy of the relativistic blast wave through internal and external shocks is the standard model for producing the prompt radiation and afterglow (see Mészáros 2006, for a recent review).

Evidence of jetted GRBs is obtained from radio (Waxman, Kulkarni & Frail 1998) and optical (Stanek et al. 1999) observations of achromatic breaks in the afterglow light curves. The structure of these jets is, however, still an open question. The two leading models are (1) the uniform jet model, in which the energy per solid angle $\partial\mathcal{E}_*/\partial\Omega$ is roughly constant within a well-defined jet opening angle θ_j , but drops sharply outside of θ_j , with θ_j differing between GRBs (see Mészáros, Rees & Wijers 1998; Mészáros & Rees 1997); and (2) the universal structured jet model (Rossi, Lazzati & Rees 2002; Zhang et al.

2004), in which all GRB jets are intrinsically identical with the directional energy release $\partial\mathcal{E}_*/\partial\Omega$ dropping approximately as the inverse square of the opening angle from the jet axis.

Frail et al. (2001) and Panaitescu & Kumar (2001) found that the absolute γ -ray energy releases, after correcting for the jet opening angles inferred from the afterglow light curves, are clustered near $\mathcal{E}_{*\gamma} \cong 5 \times 10^{50}$ ergs. Bloom et al. (2003), treating a larger sample, confirmed this clustering around $\mathcal{E}_{*\gamma} \sim 1.3 \times 10^{51}$ ergs (the total energy release $\mathcal{E}_* = \oint d\Omega (\partial\mathcal{E}_*/\partial\Omega) > \mathcal{E}_{*\gamma}$ depends on the assumed efficiency for γ -ray energy conversion). In a later analysis by Friedman & Bloom (2005), still in the pre-*Swift* era, a broader spread by about one order of magnitude is found in the beaming corrected γ -ray energy release around a mean value of $\mathcal{E}_{*\gamma} \approx 2 \times 10^{51}$ ergs (see Fig. 1). Since we use jet opening angles derived from these analyses, which are based on the uniform jet model, we also adopt this model in our treatment. The sample of Friedman & Bloom (2005) is taken to provide a good representation of the pre-*Swift* observations of GRBs. GRBs can in principle exist (e.g., Schmidt 1999; Mészáros & Mészáros 1996) and be detected to very high redshift, $z \gtrsim 10$ (Ciardi & Loeb 2000; Lamb & Reichart 2000), which holds promise that GRBs can be used to probe the early universe. Their utility for this purpose depends on the frequency and brightness of high-redshift GRBs, which in turn depends on the rate-density evolution of GRB sources and the evolution of GRB source properties with cosmic time. Given the assumption that the GRB rate density is proportional to the measured star formation rate (SFR) history of the universe (Totani 1999; Blain & Natarajan

¹ truong.le@nrl.navy.mil

² dermer@gamma.nrl.navy.mil

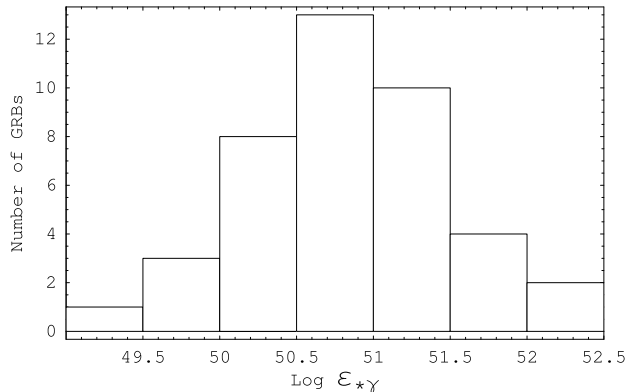


FIG. 1.— Histogram of the corrected absolute γ -ray energy release $E_{*\gamma}$ for pre-*Swift* GRBs (Friedman & Bloom 2005).

2000), the redshift distribution of GRBs can be predicted (Bromm & Loeb 2002). Correlations between spectral properties and energy releases may also permit GRBs to be used to determine cosmological parameters (e.g., Ghirlanda et al. 2004; Mortsell & Sollerman 2005).

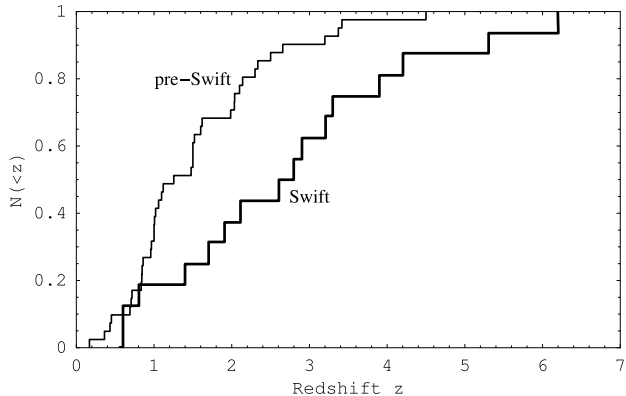


FIG. 2.— The cumulative redshift distribution of GRBs for 41 GRBs in the pre-*Swift* sample (thin histograms; Friedman & Bloom 2005), and 16 GRBs in the *Swift* sample (thick histograms; Jakobsson et al. 2006). The median redshifts of the pre-*Swift* and *Swift* bursts are $z \approx 1.25$ and $z \approx 2.70$, respectively.

With the launch of the *Swift* satellite (Gehrels et al. 2004), rapid follow-up studies of GRBs triggered by the Burst Alert Telescope (BAT) on *Swift* became possible. A fainter and more distant population of GRBs than found with the pre-*Swift* satellites CGRO-BATSE, BeppoSAX, INTEGRAL, and HETE-2 is detected (Berger et al. 2005). The mean redshift of 41 pre-*Swift* GRBs that also have measured beaming breaks (Friedman & Bloom 2005) is $\langle z \rangle = 1.5$, while 16 GRBs discovered by *Swift* have $\langle z \rangle = 2.72$ (Jakobsson et al. 2006) (see Fig. 2). Bagoly et al. (2006) performed five different statistical tests to compare the redshift distributions of *Swift* and pre-*Swift* GRBs assuming, as the null hypothesis, that they are identical distributions. They conclude that the redshift distributions are different, that is, all five tests reject the null hypothesis at the $\geq 97\%$ significance level. Thus, the pre-*Swift* and *Swift* data sample distinct subsets of the overall GRB population due to different detector characteristics and followup capabilities.

Here, we develop a physical model to understand the differences between the redshift distributions of *Swift* and pre-*Swift* GRBs, taking into account the different detector triggering properties. The GRB model is based on the uniform jet model for GRBs, though the typical properties are assigned in accordance with GRB observations. The GRB rate density and distribution of jet opening angles are the principle unknowns, with parameter values for the mean intrinsic duration and absolute γ -ray energy release of GRBs determined from observations and best fits to the data. A GRB is detected if its flux exceeds the flux threshold within the energy window of a detector (the actual detection criteria are more complicated; see Band 2003, 2006, and discussion below). For a given rate density of GRBs, the redshift and opening angle distributions are calculated and fit to the data.

We consider only data for the long, soft population of GRBs. The separation of the long duration GRBs from the short, hard GRBs, which clearly comprise a separate source population is complicated both by the extended emission observed with *Swift* from GRBs that would normally be classified as short hard GRBs (e.g., Barthelmy et al. 2005), and the appearance of the unusual GRB 060614 that defies simple classification (Gehrels et al. 2006; Gal-Yam et al. 2006; Fynbo et al. 2006). We therefore additionally assume that the data set used to test our model represents only, or mostly, classical long duration GRBs. We return to this point in the discussion.

In § 2, we develop the formulation for bursting sources, and we fit the data in § 3. Inferences for the differences between the *Swift* and pre-*Swift* redshift distributions are also made in § 3, including implications for beaming factors and low- z GRBs. We conclude in § 4 by discussing the derived GRB source rate density, the nature of the low-redshift GRBs with weak energies, and the predicted fraction of high-redshift GRBs. Derivation of the bursting rate of sources in a flat Λ cold dark matter cosmology is given in the Appendix.

2. STATISTICS OF COSMOLOGICAL GRBS

2.1. Model GRB

We approximate the spectral and temporal profiles of a GRB occurring at redshift z by an emission spectrum that is constant for observing angles $\theta = \arccos \mu \leq \theta_j = \arccos \mu_j$ to the jet axis during the period Δt_* ; thus the duration of the GRB in the observer's frame is simply $\Delta t = (1+z)\Delta t_*$ (stars refer to the stationary frame, and terms without stars refer to observer quantities). The νF_ν spectrum is therefore written as

$$\nu F_\nu \equiv f_\epsilon(t) \cong f_{\epsilon_{pk}} S(x) H(\mu; \mu_j, 1) H(t; 0, \Delta t), \quad (1)$$

where the spectral function $S(x) = 1$ at $x = \epsilon/\epsilon_{pk} = \epsilon_*/\epsilon_{pk*}$. At observer time t , $\epsilon = h\nu/m_e c^2$ is the dimensionless energy of a photon in units of the electron rest-mass energy, and ϵ_{pk} is the photon energy at which the energy flux f_ϵ takes its maximum value $f_{\epsilon_{pk}}$. The quantity $H(\mu; \mu_j, 1)$ is the Heaviside function such that $H(\mu; \mu_j, 1) = 1$ when $\mu_j \leq \mu \leq 1$, that is, the angle θ of the observer with respect to the jet axis is within the opening angle of the jet, and $H(\mu; \mu_j, 1) = 0$ otherwise. One possible approximation to the GRB spectrum is a

broken power law, so that

$$S(x) = \left[\left(\frac{\epsilon}{\epsilon_{pk}} \right)^a H(\epsilon_{pk} - \epsilon) + \left(\frac{\epsilon}{\epsilon_{pk}} \right)^b H(\epsilon - \epsilon_{pk}) \right], \quad (2)$$

where the Heaviside function $H(u)$ of a single index is defined such that $H(u) = 1$ when $u \geq 0$ and $H(u) = 0$ otherwise. The νF_ν spectral indices are denoted by $a(> 0)$ and $b(< 0)$. Note that $S(x)$ can easily be generalized to accommodate spectral energy distributions (SEDs) with multiple components.

The bolometric fluence of the model GRB for observers with $\theta \leq \theta_j$ is given by

$$F = \int_{-\infty}^{\infty} dt \int_0^{\infty} d\epsilon \frac{f_\epsilon(t)}{\epsilon} = \lambda_b f_{\epsilon_{pk}} \Delta t, \quad (3)$$

where λ_b is a bolometric correction to the peak measured νF_ν flux. If the SED is described by eq. (2), then $\lambda_b = (a^{-1} - b^{-1})$, and is independent of ϵ_{pk} . The beaming-corrected γ -ray energy release $\mathcal{E}_{*\gamma}$ for a two-sided jet is given by

$$\mathcal{E}_{*\gamma} = 4\pi d_L^2 (1 - \mu_j) \frac{F}{1 + z}, \quad (4)$$

where the luminosity distance

$$d_L(z) = \frac{c}{H_0} (1 + z) \int_0^z \frac{dz'}{\sqrt{\Omega_m (1 + z')^3 + \Omega_\Lambda}} \quad (5)$$

for a Λ CDM universe. Substituting eq. (3) for F into eq. (4) gives the peak flux

$$f_{\epsilon_{pk}} = \frac{\mathcal{E}_{*\gamma}}{4\pi d_L^2(z) (1 - \mu_j) \Delta t_* \lambda_b}. \quad (6)$$

Finally, by substituting eq. (6) into eq. (1), the energy flux becomes

$$f_\epsilon(t) = \frac{\mathcal{E}_{*\gamma} H(\mu; \mu_j, 1) H(t; 0, \Delta t) S(x)}{4\pi d_L^2(z) (1 - \mu_j) \Delta t_* \lambda_b}. \quad (7)$$

Because of the reduced spectral sensitivity of Swift to high-energy ($\gtrsim 200$ keV) emission and the measurement of ϵ_{pk} in many GRBs, and to avoid complications from the potentially large number of parameters in our GRB model, we consider in this paper the simplest GRB SED with $a = b = 0$, so that $\lambda_b \rightarrow \ln(x_{\max}/x_{\min})$ (see eqs. [3], [6] and [7]). The flat part of the spectrum takes the value of peak flux $f_{\epsilon_{pk}}$ given by eq. (6), and is assumed to intersect the sensitive range of the GRB detector. By making the above approximation, we modify the fractional number of bursts that occurs within a given redshift z and within a jet opening angle θ_j (see eqs. [18], [19], and [21]); however, the physical interpretation of the problem is expected not to change drastically when $a, b \neq 0$, which we plan to address in a subsequent paper. In the flat spectrum approximation, a νF_ν spectrum ($a = b = 0$) has to be cut off at low (x_{\min}) and high (x_{\max}) energies in order to avoid divergent flux. The model spectrum is not likely to extend over more than two orders of magnitude, so that $\lambda_b \lesssim 5$. Thus we take λ_b , the bolometric correction factor, equal to 5 in our calculations.

2.2. Bursting Rate of GRB Sources

To calculate the redshift and the jet opening angle distributions, we need to determine the rate at which GRBs occur per steradian. For a Λ CDM cosmology with $\Omega_m = 0.27$, $\Omega_\Lambda = 0.73$, and $H_0 = 72$ km s⁻¹ Mpc⁻¹ (Spergel et al. 2003), the event rate per unit time per sr for bursting sources is

$$\frac{d\dot{N}}{d\Omega} = \frac{c}{H_0} d_L^2(z) \dot{n}_{co}(\mathcal{E}_{*\gamma}, \mu_j, \epsilon_{pk*}, \Delta t_*, z) \times \frac{d\mathcal{E}_{*\gamma} d\mu_j d\mu d\epsilon_{pk*} d(\Delta t_*) dz}{(1 + z)^3 \sqrt{\Omega_m (1 + z)^3 + \Omega_\Lambda}}, \quad (8)$$

(derivation of this result is given in Appendix A). Here, $\dot{n}_{co}(\mathcal{E}_{*\gamma}, \mu_j, \epsilon_{pk*}, \Delta t_*, z) = \dot{n}_{co}(z) Y(\mathcal{E}_{*\gamma}, \mu_j, \epsilon_{pk*}, \Delta t_*)$ is the distribution of GRB sources differential in $\mathcal{E}_{*\gamma}$, μ_j , ϵ_{pk*} , Δt_* , and z , and separability of the comoving rate density $\dot{n}_{co}(z) = \dot{n}_{co} \Sigma_{SFR}(z)$ of GRBs from their properties is assumed, where $\Sigma_{SFR}(z)$ is GRB star formation rate function. This is the crucial assumption of this treatment, and so needs restated. There is assumed to be no evolution of the emission properties of GRB with cosmic time. Thus, for example, the mean jet opening angles, the mean energies, and the mean values of ϵ_{pk*} (which could be correlated with $\mathcal{E}_{*\gamma}$ to satisfy the Amati et al. (2002) and Ghirlanda et al. (2004) relations when $a, b \neq 0$) do not change through cosmic time. The phenomenological validity of the the Amati and Ghirlanda relations for GRBs at different values of z suggests the plausibility of this assumption. These relations can be introduced in more detailed treatments by considering source spectral properties where ϵ_{pk*} is correlated with $\mathcal{E}_{*\gamma}$.

Employing an integral formulation for beamed sources (Dermer 1992, 2006), the observed directional event rate for bursting sources³ with νF_ν spectral flux greater than \hat{f}_ϵ at observed photon energy ϵ is given by

$$\begin{aligned} \frac{d\dot{N}(> \hat{f}_\epsilon)}{d\Omega} &= \frac{c}{H_0} \int_{\hat{f}_\epsilon}^{\infty} df'_\epsilon \int_0^{\infty} d\mathcal{E}_{*\gamma} \int_0^{\infty} d\epsilon_{pk*} \int_0^{\infty} d(\Delta t_*) \\ &\times \int_{\mu_{j\min}}^{\mu_{j\max}} d\mu_j \int_{\mu_j}^1 d\mu \int_0^{\infty} dz \frac{d_L^2(z) \dot{n}_{co}(z) Y(\mathcal{E}_{*\gamma}, \mu_j, \epsilon_{pk*}, \Delta t_*)}{(1 + z)^3 \sqrt{\Omega_m (1 + z)^3 + \Omega_\Lambda}} \\ &\times \delta \left[f'_\epsilon - f_\epsilon(z, \mathcal{E}_{*\gamma}, \mu_j, \epsilon_{pk*}, \Delta t_*) \right]. \end{aligned} \quad (9)$$

This expression can also be written in terms of a Heaviside function involving a minimum flux threshold condition $f_\epsilon \geq \hat{f}_\epsilon$. For discrete values of $\mathcal{E}_{*\gamma}$, ϵ_{pk*} , and Δt_* ,

$$Y(\mathcal{E}_{*\gamma}, \mu_j, \epsilon_{pk*}, \Delta t_*) = g(\mu_j) \delta(\mathcal{E}_{*\gamma} - \mathcal{E}_{*\gamma 0}) \delta(\epsilon_{pk*} - \epsilon_{pk* 0}) \times \delta(\Delta t_* - \Delta t_{*0}), \quad (10)$$

where $g(\mu_j)$ is the jet opening angle distribution, and \hat{f}_ϵ is the instrument's detector sensitivity. The sensitivity of a detector to a GRB depends on many factors,

³ In a more accurate treatment of detector response, one should calculate a photon-energy integration over the energy-dependent effective area, rather than describing a γ -ray telescope by a νF_ν flux sensitivity \hat{f}_ϵ by the mean photon energy ϵ of the sensitive waveband of the detector. A further complication, not considered here, is that \hat{f}_ϵ may depend on the duration Δt of the GRB.

namely, the detector area, the detector efficiency, the fraction of the detector that is active, the fraction of the coded mask that is open, the average solid angle, and the internal background (Band 2003). Gehrels et al. (2004) give the BAT's instrument detector sensitivity to be about $\sim 10^{-8}$ ergs cm^{-2} s^{-1} , which is about an order of magnitude more sensitive than BATSE and Beppo-SAX, particularly in the case of those GRBs for which redshifts were obtained, as discussed below.

We can make a rough estimate of the detector threshold for both *Swift* and pre-*Swift* instruments, noting that the mean flare size $\langle \phi \rangle = u\phi_{\min}/(u-1)$ for a power law size distribution with index u (> 1 ; $u = 3/2$ for a Euclidean distribution). For *Swift* GRBs, we took the ratio of the measured GRB fluences to their $\langle t_{90} \rangle$ durations⁴ to find that the mean flux of a detected *Swift* GRB is $\sim 5 \times 10^{-8}$ ergs cm^{-2} s^{-1} . For an index $u \cong 1.1 - 1.2$, as appropriate to the *Swift* range, we find that the *Swift* is sensitive to GRBs as weak as 10^{-8} ergs cm^{-2} s^{-1} . We take this energy flux as the effective *Swift* flux threshold, recognizing that the actual detection of GRBs with *Swift* is more complicated, involving both a rate and image trigger (Band 2006).

The assignment of an effective flux threshold for the pre-*Swift* detectors is complicated by the fact that they involve a variety of detectors—BATSE, Beppo-SAX, HETE-II, and INTEGRAL—each with its own specific triggering criteria. The mean flux of the pre-*Swift* sample can be obtained from the values of fluence and t_{90} compiled by Friedman & Bloom (2005). We find that the mean flux of the pre-*Swift* GRBs is $\sim 7 \times 10^{-7}$ ergs cm^{-2} s^{-1} , meaning that the flux threshold sensitivity is a factor ≈ 5 less than this value, because $u \cong 1.2$ at fluxes $\gtrsim 10^{-7}$ ergs cm^{-2} s^{-1} (Paciesas et al. 1999). For simplicity, we use the value of 10^{-7} ergs cm^{-2} s^{-1} for the mean sensitivities of the GRB detectors prior to *Swift*. Hence, in this work we assume the detector threshold for *Swift* and pre-*Swift* GRBs to be $\sim 10^{-8}$ and $\sim 10^{-7}$ ergs cm^{-2} s^{-1} , respectively.

Integrating over μ in eq. (9) gives the factor $(1 - \mu_j)$ describing the rate reduction due to the finite jet opening angle. Hence, eq. (9) becomes

$$\frac{d\dot{N}(> \hat{f}_\epsilon)}{d\Omega} = \frac{c}{H_0} \int_{\hat{f}_\epsilon}^{\infty} df'_\epsilon \int_{\mu_{j\min}}^{\mu_{j\max}} d\mu_j g(\mu_j)(1 - \mu_j) \times \int_0^{\infty} dz \frac{d_L^2(z) \dot{n}_{co}(z) \delta(f'_\epsilon - f_\epsilon)}{(1+z)^3 \sqrt{\Omega_m(1+z)^3 + \Omega_\Lambda}}, \quad (11)$$

where f_ϵ is given by eq. (7).

In order to close the system of equations and solve for the redshift distribution, we must also specify the functional form of $g(\mu_j)$ as well as the comoving GRBs rate density $\dot{n}_{co}(z)$. GRBs with small opening angles, that is, with $\theta_j \ll 1$, will radiate their available energy into a small cone, so that such GRBs are potentially detectable from larger distances (though not always, as a different portion of the spectrum is observed), with their rate reduced by the factor $(1 - \mu_j)$. By contrast, GRB jets with large opening angles are more frequent but only detectable from comparatively small distances. The

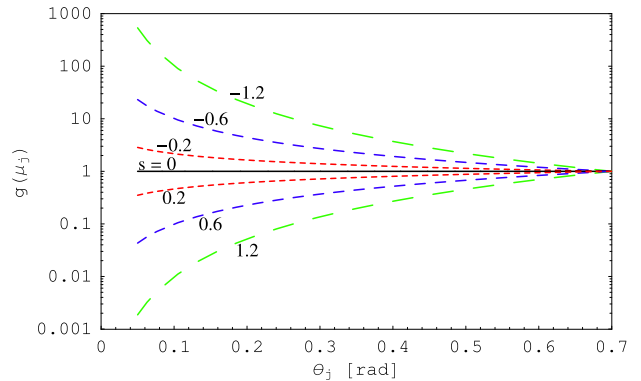


FIG. 3.— The number of sources per unit θ_j angle for $s = -1.2, -0.6, -0.2, 0, 0.2, 0.6, 1.2$ in eq. (12) between $\theta_j = 0.05$ and 0.7 radians.

intrinsic opening angle distribution can be much different than the measured opening-angle distribution because of these effects (Guetta, Piran, & Waxman 2005).

Since the form for the jet opening angle $g(\mu_j)$ is unknown, we consider the function

$$g(\mu_j) = g_0 (1 - \mu_j)^s H(\mu_j; \mu_{j\min}, \mu_{j\max}), \quad (12)$$

where s is the jet opening angle power-law index; for a two-sided jet, $\mu_{j\min} \geq 0$. Because the distributions are normalized to unity,

$$g_0 = \frac{1 + s}{(1 - \mu_{j\min})^{1+s} - (1 - \mu_{j\max})^{1+s}}. \quad (13)$$

Equation (12) hardly exhausts the possible expressions for $g(\mu_j)$, but contains interesting asymptotic behaviors. In Figure 3, we illustrate the nature of this function by fixing the range of the jet opening angle for different value of s . Here we take θ_j lying between 0.05 and 0.7 radians ($\approx 2.8^\circ - 40^\circ$). This figure shows that the fraction of bursts with small jet opening angles $\theta_j \ll 1$ increases with decreasing values of $s < 0$. Therefore most bursts have large jet opening angle when $s > 0$. Since beaming effects are only important for negative s , and because beaming effects are certainly important for GRBs, we only consider negative value of s in our analysis. Furthermore, from equation (13) it is clear that if $s \leq -1$, it is necessary to have a minimum opening angle $\theta_j = \arccos \mu_j > 0$ in order to avoid a divergent fraction of GRBs with small jet opening angles. Note also that $g(\mu_j)$, eq. (12), approaches a δ -function when $\mu_{j\min} \rightarrow \mu_{j\max}$.

It has been suggested (e.g., Totani 1997; Natarajan et al. 2005) that the GRB formation history is expected to follow the cosmic SFR (Σ_{SFR}) derived from the blue and UV luminosity density of distant galaxies, though with differences related to the metallicity dependence and fraction of the subset of high-mass stars that are GRB progenitors. However, as we show in § 3, in order to obtain the best fit to the *Swift* redshift and the pre-*Swift* redshift and jet opening angle samples, we have to employ a GRB formation history that displays a monotonic increase in the SFR at high redshifts (SFR5 and SFR6; see Fig. 4). To investigate the nature of the GRB formation history, in this work we also assume that $\dot{n}_{co}(z) \propto \Sigma_{\text{SFR}}(z)$, and

⁴ swift.gsfc.nasa.gov

consider specific functional forms for $\Sigma_{\text{SFR}}(z)$. Due to the large range of uncertainties in the SFR at $z \gtrsim 1$, we first consider three different functional forms for the SFR. For the lower SFR (LSFR) and upper SFR (USFR) that should bound the actual SFR, we consider the analytic function

$$\Sigma_{\text{SFR}}(z) = \frac{1 + a_1}{(1+z)^{-a_2} + a_1(1+z)^{a_3}}, \quad (14)$$

(Wick, Dermer & Atoyan 2004), with $a_1 = 0.005(0.0001)$, $a_2 = 3.3(4.0)$, and $a_3 = 3.0(3.0)$ for the LSFR (USFR). The LSFR (SFR2) and USFR (SFR4) describe extreme ranges of optical/UV measurements without and with dust extinction (Blain et al. 1999) corrections, respectively. We also consider the SFR history (SFR3) of Hopkins & Beacom (2006), which is intermediate between the LSFR and USFR, using their analytic fitting profile given by

$$\Sigma_{\text{SFR}}(z) = \frac{1 + (a_2 z/a_1)}{1 + (z/a_3)^{a_4}}, \quad (15)$$

where $a_1 = 0.015$, $a_2 = 0.10$, $a_3 = 3.4$, and $a_4 = 5.5$ are their best fit parameters⁵. Figure 4 shows these SFR functions, with the function normalized to unity at the present epoch $z = 0$. The constant comoving density, SFR1, is also plotted. Note that SFR2, SFR3,

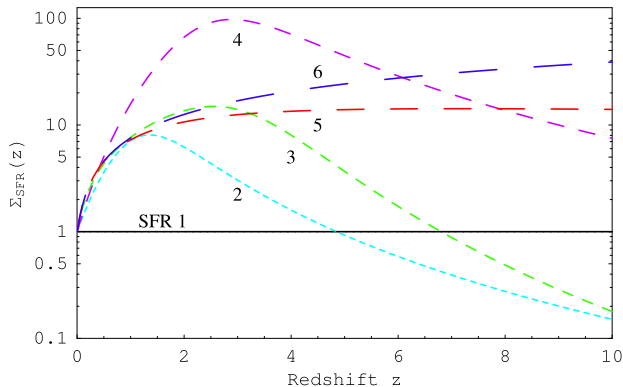


FIG. 4.— Star formation rate (SFR) function for GRBs, assumed to be proportional to comoving SFR histories as shown. The solid line (SFR1) is a constant comoving density; SFR2 and SFR4 are the lower and upper SFRs given by eq. (13); SFR3 is the Hopkins & Beacom (2006) SFR history given by eq. (14), with ($a_1 = 0.015$, $a_2 = 0.1$, $a_3 = 3.4$, $a_4 = 5.5$); and SFR5 ($a_1 = 0.015$, $a_2 = 0.12$, $a_3 = 3.0$, $a_4 = 1.3$) and SFR6 ($a_1 = 0.011$, $a_2 = 0.12$, $a_3 = 3.0$, $a_4 = 0.5$) are the SFRs that give a good fit to the *Swift* and pre-*Swift* redshift distribution.

and SFR4 are similar when $z \lesssim 1$, but differ greatly at higher redshifts. We also consider two alternative functions shown in Fig. 4, SFR 5 and SFR6, that display a monotonic increase in the SFR at high redshifts representing positive evolution of the SFR history of the universe to $z \gtrsim 5$. Later in the analysis we will show that for self-consistency we have to utilize SFR5 and SFR6 instead of SFR2, SFR3, and SFR4, to obtain the best fit

⁵ Adjustments to these values in later versions of the paper by Hopkins & Beacom (2006) produce negligible differences in our results.

to the *Swift* redshift, and the pre-*Swift* redshift and jet opening angle samples.

2.3. Redshift, Size, and Jet Opening Angle Distributions

The directional GRB rate per unit redshift with energy flux $> \hat{f}_\epsilon$ is thus given by

$$\frac{d\dot{N}(> \hat{f}_\epsilon)}{d\Omega dz} = \frac{cg_0}{H_0(2+s)} \frac{d_L^2(z) \dot{n}_{co}(z)}{(1+z)^3 \sqrt{\Omega_m(1+z)^3 + \Omega_\Lambda}} \times \{[1 - \max(\hat{\mu}_j, \mu_{j\min})]^{2+s} - (1 - \mu_{j\max})^{2+s}\}, \quad (16)$$

after substituting eq. (12) into eq. (11) and solving; here

$$\hat{\mu}_j \equiv 1 - \frac{\mathcal{E}_{*\gamma}}{4\pi d_L^2(z) \Delta t_* \hat{f}_\epsilon \lambda_b}. \quad (17)$$

When $f_\epsilon = \hat{f}_\epsilon$, where \hat{f}_ϵ is the νF_ν flux threshold sensitivity of a GRB telescope that observes in a waveband centered at $\epsilon = \bar{\epsilon}$, eq. (16) gives the redshift distribution. The size distribution of GRBs in terms of their νF_ν flux f_ϵ is then simply

$$\frac{d\dot{N}(> \hat{f}_\epsilon)}{d\Omega} = \frac{cg_0}{H_0(2+s)} \int_0^{z_{\max}} dz \frac{d_L^2(z) \dot{n}_{co}(z)}{(1+z)^3 \sqrt{\Omega_m(1+z)^3 + \Omega_\Lambda}} \times \{[1 - \max(\hat{\mu}_j, \mu_{j\min})]^{2+s} - (1 - \mu_{j\max})^{2+s}\}. \quad (18)$$

The maximum redshift z_{\max} can be obtained by solving the luminosity distance $d_L(z)$ using equation (17) to obtain

$$d_L^2(z_{\max}) \leq \frac{\mathcal{E}_{*\gamma}}{4\pi(1 - \mu_{j\min}) \Delta t_* \hat{f}_\epsilon \lambda_b}. \quad (19)$$

Finally, the jet opening angle distribution (see eq. [11]) is given by

$$\frac{d\dot{N}(> \hat{f}_\epsilon)}{d\Omega d\mu_j} = \frac{c}{H_0} g(\mu_j)(1 - \mu_j) \times \int_0^{z_{\max}(\mu_j)} dz \frac{d_L^2(z) \dot{n}_{co}(z)}{(1+z)^3 \sqrt{\Omega_m(1+z)^3 + \Omega_\Lambda}}, \quad (20)$$

where $g(\mu_j)$ is given in equations (12) and (13), and the upper limit of the redshift integration is determined by equation (19).

3. RESULTS

In our GRB model, there are seven adjustable parameters: the νF_ν spectral power-law indices a and b , the power-law index s of the jet opening-angle distribution, the range of the jet opening angles $\theta_{j\min}$ and $\theta_{j\max}$, the absolute emitted γ -ray energy $\mathcal{E}_{*\gamma}$, and the detector threshold \hat{f}_ϵ . As already mentioned, we consider, for simplicity, a flat νF_ν GRB SED, so that $a = b = 0$, leaving only the bolometric correction factor λ_b , which is set equal to 5. The remaining parameters $\theta_{j\min}$, $\theta_{j\max}$, s , and $\mathcal{E}_{*\gamma}$ are constrained by observations, and the detector properties are used to estimate \hat{f}_ϵ .

Besides these parameters, we must also assume a GRB comoving rate density $\dot{n}_{co}(z) = \dot{n}_{co} \Sigma_{\text{SFR}}(z)$, which is also constrained by fitting our model to the observed data. Adopting the uniform jet model, we assume that

the energy per solid angle is roughly constant within the well-defined jet opening angle (e.g., Frail et al. 2001; Bloom et al. 2003). With these assumptions, we investigate the behavior of the redshift and opening angle distributions. Before we proceed to compare our model of redshift and jet opening angle distributions with the samples obtained by the *Swift* and pre-*Swift* instruments, we need to explore some of the above parameter space.

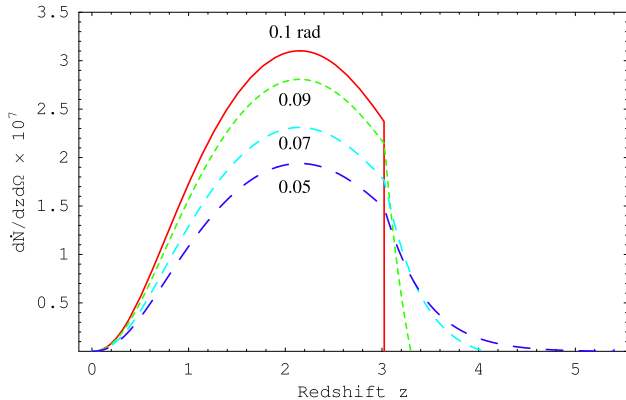


FIG. 5.— Directional event rate per unit redshift [one event per $(10^{28} \text{ cm})^3$ per day per *sr* per z] for an assumed δ -function distribution of the jet opening angles, so that $g(\mu_j) = \delta(\mu_j - \hat{\mu}_j)$, with $\hat{\theta}_j = 0.1$ radian (solid-curve), using SFR3 and $\hat{f}_{\bar{\epsilon}} = 10^{-7} \text{ ergs cm}^{-2} \text{ s}^{-1}$. Also shown are the directional event rates with $\theta_{j\text{max}} = 0.1$ radian, and $\theta_{j\text{min}} = 0.05, 0.07,$ and 0.09 radians, with $s = 0$.

3.1. Parameter Study of GRB Model

For illustrative purposes, we utilize SFR3 (Hopkins & Beacom 2006) for the GRB comoving rate density. Furthermore, we also assume that $s = 0$, $\theta_{j\text{min}} = \theta_{j\text{max}} = \theta_j = 0.1$ radian (this assumption implies $g(\mu_j)$ is a δ -function, see eqs. [11], [12], and Fig. 5), $\Delta t_* = 10 \text{ s}$, $\mathcal{E}_{*\gamma} = 2 \times 10^{51} \text{ ergs}$, and $\hat{f}_{\bar{\epsilon}} = 10^{-8}$ and $10^{-7} \text{ ergs cm}^{-2} \text{ s}^{-1}$ for the flux sensitivity of detectors for *Swift* and before *Swift*, respectively. We choose $\Delta t_* = 10 \text{ s}$, and $\mathcal{E}_{*\gamma} = 2 \times 10^{51} \text{ ergs}$ because these are the mean values of the GRB duration measured with BATSE assuming that BATSE GRBs are typically at $z \approx 1$, and the mean beaming corrected γ -ray energy release (see Fig. 1), respectively. We shall use $\Delta t_* = 10 \text{ s}$ throughout this work. The calculation is normalized to a local ($z \ll 1$) event rate of one GRB per day per $(10^{28} \text{ cm})^3$, so that the normalization of the local rate density is $\dot{n}_{co} = 1.157 \times 10^{-89} \text{ cm}^{-3} \text{ s}^{-1}$.

With the jet opening angle $\theta_j = 0.05$ and $\theta_j = 0.1$ radians, and the detector threshold $\hat{f}_{\bar{\epsilon}} = 10^{-7} \text{ ergs cm}^{-2} \text{ s}^{-1}$, the maximum redshifts from which model GRBs could be detected are $z_{\text{max}} = 5.4$ and 3.02 , respectively (see eq. [19]). The directional event rate per unit redshift is shown in Figure 5. Setting $\theta_{j\text{max}} = 0.1$ radian, and $\theta_{j\text{min}} = 0.05, 0.07, 0.09$ radians (the three dashed curves in Figure 5), we plot the directional event rate per unit redshift for different values of $\theta_{j\text{min}}$ (see eq. [18]). As $\theta_{j\text{min}} \rightarrow \theta_{j\text{max}}$, the directional event rate per unit redshift of the respective $\theta_{j\text{min}}$ -curves approaches the directional event rate per redshift of the δ -function $g(\mu_j)$ with $\theta_j = 0.1$ radian. In Figure 6 we examine three different val-

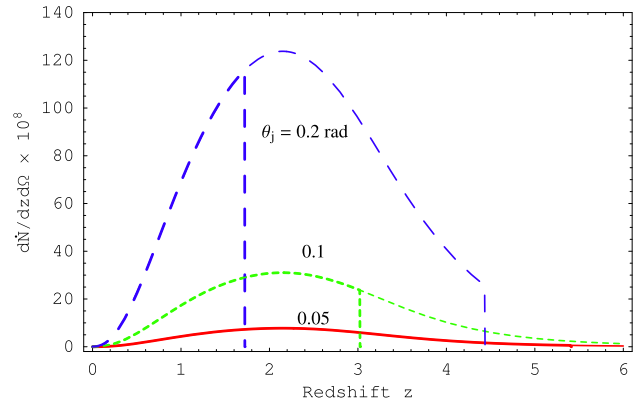


FIG. 6.— Directional event rate per unit redshift, in units of GRBs per s per sr per unit redshift z , normalized to one event per $(10^{28} \text{ cm})^3$ per day, with $\theta_j = 0.05, 0.1,$ and 0.2 radian, using SFR3. The thin and thick curves represent the instrument's energy flux sensitivity of $10^{-8} \text{ ergs cm}^{-2} \text{ s}^{-1}$ (*Swift*) and $10^{-7} \text{ ergs cm}^{-2} \text{ s}^{-1}$ (pre-*Swift*), respectively.

ues of the jet opening angle, $\theta_{j\text{min}} = \theta_{j\text{max}} = \theta_j = 0.05, 0.1,$ and 0.2 radians, with two values of flux sensitivity, namely 10^{-8} and $10^{-7} \text{ ergs cm}^{-2} \text{ s}^{-1}$. As can be seen, the smaller the jet opening angle the larger the maximum redshift from which the GRB is detectable. The maximum observable redshift z associated with a particular opening angle is indicated by the vertical line in each curve. Moreover, Figure 6 also shows that whatever the lower sensitivity telescope detects will also be detected by a telescope with better sensitivity, because a flat νF_ν spectrum is considered. Thus *Swift*, being more sensitive than earlier telescopes, would in this model detect a sample of GRBs encompassing those detected with instruments before *Swift*. Spectral behavior can be considered in more detailed treatments and will change the relations for maximum distances, though generally with better sensitivity the telescope can view to larger distances, especially when the more sensitive telescope can observe lower energy photons.

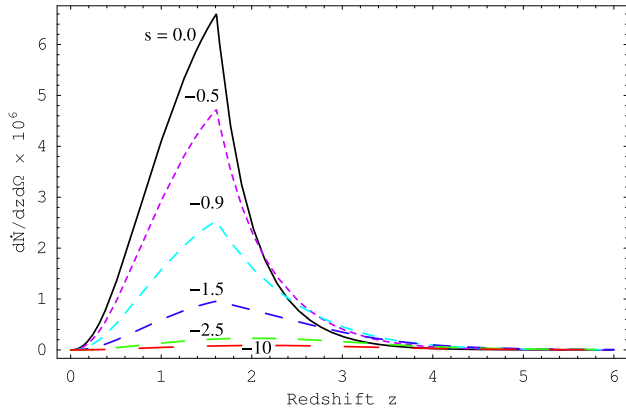


FIG. 7.— Directional event rate per unit redshift [one event per $(10^{28} \text{ cm})^3$ per day per sr per z] with $\theta_{j\text{min}} = 0.05$ rad and $\theta_{j\text{max}} = 0.7$ rad, $s = 0.0, -0.5, -0.9, -1.5, -2.5,$ and -10.0 , with SFR3 and $\hat{f}_\epsilon = 10^{-8} \text{ ergs cm}^{-2} \text{ s}^{-1}$.

By varying the opening angle power-law index parameter s over values $s = 0.0, -0.5, -0.9, -1.5, -2.5,$ and -10.0 , with $\theta_{j\text{min}} = 0.05$, $\theta_{j\text{max}} = 0.7$ radians and $\hat{f}_\epsilon = 10^{-8} \text{ ergs cm}^{-2} \text{ s}^{-1}$, while keeping all other assumed parameters as before, Figure 7 shows that the burst rate per unit redshift is progressively distributed to higher z , as expected, since the more negative s is, the larger is the fractional number of bursts that occurs at small jet-opening angles θ_j (see also Figure 3). More importantly, as $s \ll 0$, the directional event rate per unit redshift reaches an asymptotic limit (see plots for $s = -2.5$ and -10.0 in Figure 7).

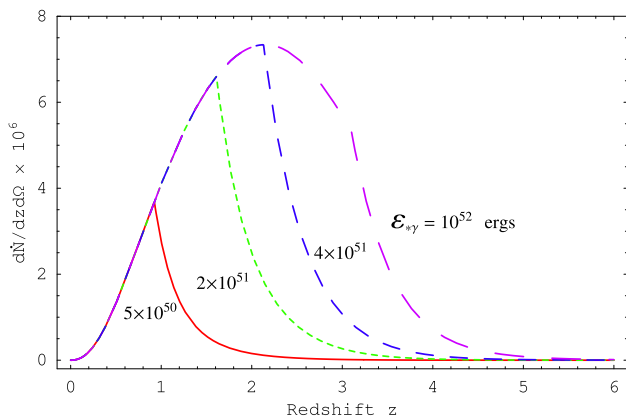


FIG. 8.— Directional event rate per unit redshift [one event per $(10^{28} \text{ cm})^3$ per day per sr per z] with $\theta_{j\text{min}} = 0.05$ rad and $\theta_{j\text{max}} = 0.7$ rad for $\mathcal{E}_{*\gamma} = 5 \times 10^{50}, 2 \times 10^{51}, 4 \times 10^{51},$ and 10^{52} ergs, using SFR3.

The final parameter that we need to explore is the corrected γ -ray energy $\mathcal{E}_{*\gamma}$. By setting $\mathcal{E}_{*\gamma} = 5 \times 10^{50}, 2 \times 10^{51}, 4 \times 10^{51},$ and 10^{52} ergs with $\theta_{j\text{min}} = 0.05$ and $\theta_{j\text{max}} = 0.7$ radians, $s = 0$, and $\hat{f}_\epsilon = 10^{-8} \text{ ergs cm}^{-2} \text{ s}^{-1}$, Figure 8 shows that as the emitted γ -ray energy increases, the bursting rate is shifted to higher z , as expected.

3.2. Parameter Fits to the Swift and pre-Swift Redshift samples

From Friedman & Bloom (2005), the pre-*Swift* jet opening angle distribution extends from $\theta_j = 0.05$ to $\theta_j = 0.6$ radians. However, other workers have reported that the observed jet-opening angles are as large as $\theta_j = 0.7$ radians (e.g., Guetta, Piran, & Waxman 2005). Hence, in this work we explore different ranges of θ_j , ranging from $\theta_{j\text{min}} = 0.05$ radians to $\theta_{j\text{max}} = \pi/2, 0.7,$ and 0.4 radians. We also use $\Delta t_* = 10$ s as the average GRB duration in the stationary frame. We first consider SFR3 (Hopkins & Beacom 2006) to fit the redshift distribution from the *Swift* and pre-*Swift* samples, and the opening angle distribution from the pre-*Swift* sample. A large number of jet opening angles associated with the *Swift* redshift sample is lacking, so our calculated jet opening angle distribution will be used as a prediction for *Swift*. As indicated in Figure 1, the corrected γ -ray energy release is broadly distributed around the mean value of $\mathcal{E}_{*\gamma} = 2 \times 10^{51}$ ergs; hence we can explore different values of γ -ray energy that best fit the observed redshift and opening angle samples. It is important, however, that the best-fit value is not too far off from the mean value in order for our model to be in accord with observations. Later in the analysis we will show that our best fit corrected γ -ray energy $\mathcal{E}_{*\gamma}$ is indeed only a factor of 2 larger than the mean.

In Figures 9, 10 and 11, we plot the calculated redshift distribution at three different corrected total γ -ray energies, $\mathcal{E}_{*\gamma} = 2 \times 10^{51}, 5 \times 10^{51},$ and 10^{52} ergs, respectively. In each panel, each curve represents the calculated cumulative redshift distribution for the power-law index s of the jet opening angle distribution. The values $s = -0.6, -1.2, -1.8,$ and -2.4 are plotted, from far left to far right, respectively. In each figure, from top to bottom, we have $\theta_{j\text{min}} = 0.05$ and $\theta_{j\text{max}} = \pi/2$ radians, $\theta_{j\text{min}} = 0.05$ and $\theta_{j\text{max}} = 0.7$ radians, and $\theta_{j\text{min}} = 0.05$ and $\theta_{j\text{max}} = 0.4$ radians, respectively, as the jet opening angles. The cumulative redshift distribution (bold solid curves) of the *Swift* and pre-*Swift* samples are plotted for comparison. We do not plot $s < -2.4$, since there is little variation in the redshift distribution (see Fig. 7). The results in Figures 9, 10, and 11 clearly show that the redshift distributions for different values of s from the model do not fit the *Swift* redshift sample. Furthermore, the fits to both the *Swift* and pre-*Swift* samples do not correlate together with the associated range of the jet opening angle. In fact it indicates that we need larger burst rates at higher redshifts ($z > 3$). These results rule out the lower SFR, SFR2, as can be seen in Figure 12.

It is important to note at this point that the fit to the pre-*Swift* and *Swift* redshift distribution should rely on a single comoving rate density of GRB with the same physical parameters. If one particular GRB rate model cannot fit the observed pre-*Swift* and *Swift* redshift distribution at the same time, then that GRB model has to be eliminated, unless additional complications are introduced into the model, such as the change of GRB model parameters with time.

The comparisons also rule out the possibility that the upper SFR explains the GRB data, even though SFR4 has a higher SFR than SFR2 at large redshifts. In Figure 13 we fit the pre-*Swift* and *Swift* redshift samples using three different γ -ray energies, namely $\mathcal{E}_{*\gamma} = 5 \times 10^{50}, 2 \times 10^{51},$ and 10^{52} ergs, with $s = -0.6, -1.2, -1.8,$ and

–2.4 using SFR4. The results for the range of the jet opening angle $\theta_{\text{jmin}} = 0.05$, and $\theta_{\text{jmax}} = 0.7$ radians show that the calculated redshift distribution between *Swift* and pre-*Swift* are anticorrelated, that is, smaller values of s , which would improve the fit for *Swift* GRBs, makes the fit for pre-*Swift* GRBs worse. However, with $s = -0.6$ and $\mathcal{E}_{*\gamma} = 10^{52}$ ergs (two bottom panels), the redshift distributions are marginally acceptable by the model, noting that the Kolmogorov-Smirnov one-sided test statistic for a sample of 41 and 31 GRBs at the 10% level are 0.167 and 0.187, respectively (that is, only 10% of randomly chosen samples should exhibit maximum vertical deviations from the model cumulative distribution; if it is greater than these values, then the model is an inadequate representation of the data at the 90% confidence level). Only 2.5% of randomly chosen samples should have vertical excursions greater than 0.212 and 0.238 for a sample of 41 and 31 GRBs, respectively.

When we calculate the opening angle distribution to fit the pre-*Swift* opening angle sample in Figure 14, however, the fit is adequate for $\mathcal{E}_{*\gamma} = 10^{52}$ ergs and $s = -1.2$ but not for $s = -0.6$. Hence, the upper SFR (SFR4) is statistically eliminated. Nevertheless, the results in Figure 13 suggest that a greater GRB burst rate at larger redshifts is required to fit the redshift distributions. The cumulative jet opening angle distribution (bold solid curves) of the pre-*Swift* sample is plotted for comparison, but not for *Swift*, since the available opening angles for the associated *Swift* redshift sample are lacking.

As a result, we consider a GRB comoving source rate density that exhibits positive evolution above redshift $z > 3$. We therefore modify the Hopkins & Beacom SFR (SFR3) to obtain the comoving rate-density that attains (1) a constant comoving rate-density at high redshift z (SFR5), and (2) a monotonically increasing comoving rate-density with increasing redshift (SFR6) in order to provide a high GRB burst rate at large z (see caption to Figure 4 for coefficients of the SFR models).

In Figures 15 and 16 we begin to see some improvement in fitting the pre-*Swift* and *Swift* redshift samples when using SFR5 and SFR6 with $\mathcal{E}_{*\gamma} = 2 \times 10^{51}$ ergs. Nevertheless, the fitting is still somewhat inconsistent between the pre-*Swift* redshift distribution and the jet opening angle. For example, in Figure 15 using SFR5, the fitting to the pre-*Swift* and *Swift* redshift distribution shows a good fit with $s = -1.2$ for a range of jet opening angles between $\theta_{\text{jmin}} = 0.05$ and $\theta_{\text{jmax}} = 0.4$ radians (two bottom panels). However, the result from the fitting between the pre-*Swift* redshift distribution and the opening angle distribution with $s = -1.2$ is inconsistent (see Figures 15 and 16). Above redshift $z > 2$, the calculated redshift distribution underestimates the fractional number of bursts that should occur at high redshifts z . On the other hand, the calculated opening angle distribution overestimates the fractional number of GRBs that should occur at small opening angles. Recall that if a burst occurs at a small opening angle, then this translates into the possibility of observing this particular burst at a high redshift z . Hence, the fit with the range of the jet opening angle $\theta_{\text{jmin}} = 0.05$, and $\theta_{\text{jmax}} = 0.4$ radians is not yet acceptable.

In Figures 17 and 18 we see similar results when using SFR6. However, it is interesting to note that we

can resolve this problem if we could increase the fractional number of GRBs at both high and low redshifts z . As a result, this will provide a self-consistent fitting between the pre-*Swift* redshift and the jet opening angle distributions, as well as the *Swift* redshift distribution. This problem can be solved by adjusting the γ -ray energy $\mathcal{E}_{*\gamma}$. Using $\mathcal{E}_{*\gamma} = 4 \times 10^{51}$ ergs, Figures 19 and 20, and Figures 21 and 22 show a statistically acceptable fit to the pre-*Swift* and *Swift* redshift distribution and the pre-*Swift* opening angle distribution with $s = -1.2$, and the range of the jet opening angle $\theta_{\text{jmin}} = 0.05$ and $\theta_{\text{jmax}} = 0.7$ radians for SFR5 and SFR6, respectively. For SFR5, the fitting can be improved with $s = -1.3$, as indicated by the solid curves (see Figures 19 and 20).

The above analyses show that $\mathcal{E}_{*\gamma} = 4 \times 10^{51}$ ergs gives the best fit to the pre-*Swift* redshift and the jet opening angle samples, and the *Swift* redshift sample. This best-fitted γ -ray energy is interesting since Frail et al. (2001) and Bloom et al. (2003) show that the standard-energy reservoir is $\mathcal{E}_{*\gamma} \cong 10^{51}$ ergs. However, with a larger sample set, the data from Friedman & Bloom (2005) shows that $\mathcal{E}_{*\gamma}$ is broadly distributed between $\mathcal{E}_{*\gamma} \sim 10^{51-52}$ ergs, as shown in Figure 1. Because we have been able to obtain an acceptable fit to the data with discrete values of $\mathcal{E}_{*\gamma}$ and Δt_* , a more complicated model where a range of values of $\mathcal{E}_{*\gamma}$ and Δt_* were allowed would certainly permit excellent fits to the data.

3.3. Estimating the Beaming Factor and the Luminosity Function

We can utilize our best-fitted parameters to estimate the average beaming factor $\langle f_b^{-1} \rangle$. The beaming factor average over the opening angle distribution is given by

$$\begin{aligned} \langle f_b \rangle &= \frac{\int_{\mu_{\text{jmin}}}^{\mu_{\text{jmax}}} (1 - \mu_j) g(\mu_j) d\mu_j}{\int_{\mu_{\text{jmin}}}^{\mu_{\text{jmax}}} g(\mu_j) d\mu_j} \\ &= \left(\frac{1+s}{2+s} \right) \left[\frac{(1 - \mu_{\text{jmin}})^{2+s} - (1 - \mu_{\text{jmax}})^{2+s}}{1 - \mu_{\text{jmin}}^{1+s} - (1 - \mu_{\text{jmax}})^{1+s}} \right], \end{aligned} \quad (21)$$

where $g(\mu_j)$ is given in equation (12). Using the best-fitted parameters $s = -1.2$ and $s = -1.3$ and the range of the jet opening angles between $\theta_{\text{jmin}} = 0.05$ and $\theta_{\text{jmax}} = 0.7$, we obtain $\langle f_b \rangle^{-1} \simeq 34 - 42$ as the beaming factor for $s = -1.2$ and $s = -1.3$, respectively. Our value of $\langle f_b \rangle^{-1}$ is about a factor of 2 smaller than the value obtained by Guetta, Piran, & Waxman (2005).

We can also infer the luminosity function from the jet opening angle distribution. From equations (8) and (9), the jet opening angle distribution is $d\dot{N}/d\mu_j = g(\mu_j)$, which is related to luminosity by the expression

$$\frac{d\dot{N}}{dL_*} = g(\mu_j) \left| \frac{d\mu_j}{dL_*} \right|, \quad (22)$$

where L_* is the GRB apparent isotropic luminosity, and $g(\mu_j)$ is the jet opening angle distribution given in equation (12). Since the energy flux is defined as $\Phi_E = L_*/4\pi d_L^2$ or $f_\epsilon = \nu F_\nu = \nu_* L_{\nu_*}/4\pi d_L^2$, then the isotropic luminosity in the bursting frame is $L_* = \nu_* L_{\nu_*}$, so that $L_* = 4\pi d_L^2 f_\epsilon$. Utilizing equation (17), the jet opening angle in terms of isotropic luminosity is given

by

$$\mu_j = 1 - \frac{\mathcal{E}_{*\gamma}}{\Delta t_* \lambda_b L_*}. \quad (23)$$

Substituting equation (23) into equation (22), we obtain $dN/dL_* \propto L_*^{-(s+2)}$ after utilizing the jet opening angle distribution in equation (12). Since our best fit to the pre-*Swift* redshift and opening angle samples and the *Swift* redshift sample constrains the jet opening angle distribution power-law index s between -1.3 and -1.2 for using SFR5 and SFR6, respectively, our apparent isotropic luminosity function is $\propto L_*^{-3.25}$ within the uniform jet model. In the universal structured jet model, the luminosity function is suggested to be $\propto L_*^{-2}$ (e.g., Guetta, Piran, & Waxman 2005; Perna, Sari, & Frail 2003); others have suggested that the luminosity function is $\propto L_*^{-2.3}$ (e.g., Lloyd-Ronning, Fryer, & Ramirez-Ruiz 2002). For our best fitting model with jet opening angles ranging from $\theta_j = 0.05$ to $\theta_j = 0.7$ rad, this implies bolometric γ -ray luminosities in the range $\approx 2 \times 10^{51}$ to $\approx 3 \times 10^{53}$ ergs s^{-1} .

The results for our best fitting model are shown in Figure 23. The fraction of high-redshift GRBs in the high-redshift universe implied by our fits using SFR5 and SFR6 is estimated at $8 - 12\%$ and $2.5 - 6\%$ at $z \geq 5$ and $z \geq 7$, respectively. If this fraction is not observed with *Swift*, then it suggests that SFR5 and SFR6 do not continue with positive evolution $z \gg 5$. Indeed, it is likely that the formation rate of GRBs at high redshift declines at sufficiently high redshift. We can also derive the fractional number of GRBs with $z \leq 0.25$ from Figure 23. We find that $\lesssim 0.2\%$ of long duration GRBs should occur in the low-redshift ($z \leq 0.25$) universe.

4. DISCUSSION AND CONCLUSIONS

In this work, we considered whether the differences between the pre-*Swift* and *Swift* redshift distributions can be explained with a physical model for GRBs that takes into account the different flux thresholds of GRB detectors. The model presented here parameterizes the jet opening angle distribution for an assumed flat νF_ν spectrum, and finds best fit values for the γ -ray energy release for different functional forms of the comoving rate density of GRBs, assuming that the properties of GRBs do not change with time. Adopting the uniform jet model, we assumed that the energy per solid angle is roughly constant within a well-defined jet opening angle. The pre-*Swift* redshift sample suggests that the range of the jet opening angle is between 0.05 and 0.7 radians. We explored three different ranges of jet opening angle with $\theta_{j\min} = 0.05$, and $\theta_{j\max} = \pi/2$, 0.7 , and 0.4 radians.

The results in § 3 show that an intrinsic distribution in the jet opening angles and single values for all other parameters yields a good fit to the pre-*Swift* and *Swift* redshift samples, and furthermore provides an acceptable fit to the distribution of opening angles measured with pre-*Swift* GRB detectors. A good fit was only possible, however, by modifying the Hopkins & Beacom SFR to provide positive evolution of the SFR history of GRBs to high redshifts (SFR5 and SFR6; see Fig. 4). The best fit values were obtained with $\mathcal{E}_{*\gamma} = 4 \times 10^{51}$ ergs, $\theta_{j\min} = 0.05$, $\theta_{j\max} = 0.7$ radians, and $s \cong -1.25$. The

best-fit value for the absolute γ -ray energy released by a GRB is about a factor of 2 larger than the mean value of the Friedman & Bloom (2005) sample of pre-*Swift* GRBs.

The results of our fitting therefore indicate that GRB activity was greater in the past and is not simply proportional to the bulk of the star formation as traced by the blue and UV luminosity density of the universe. This is contrary to the conclusion of Porciani & Madau (2001) based upon a study of BATSE size distribution and a small number of GRBs with known redshifts in the pre-*Swift* era. They obtain worse fits for SFRs that increase at high redshift. The BATSE analysis of Mészáros et al. (2006) gives results that are consistent with the required monotonically increasing GRB SFR that we find. Daigne et al. (2006) also conclude that a rising GRB SFR is implied, and also note that the star formation rate cannot increase in proportion to greater past GRB activity, as this would result in overproduction of metals. Changes in the progenitor population or GRB properties, for example, due to changing metallicities with time, might account for the large number of high-redshift GRBs observed with *Swift*, but this would introduce a large number of unconstrained parameters. Moreover, one would then have to explain why the Amati and Ghirlanda correlations relating spectral properties and energy releases are insensitive to redshift.

Assuming that the GRB properties do not change with time, we therefore find that the GRB source rate density must display positive evolution to at least $z \gtrsim 5$. Why would GRB activity be greater in the past? One possibility suggested by recent studies (Stanek et al. 2006; Fruchter et al. 2006) on the metallicities of host galaxies of GRBs is that GRBs derive from progenitor stars with a lower metallicity than the progenitors of Type II SNe. In this case, one might expect that the peak of GRB activity would occur earlier in the universe than during the peak of star formation activity at $z \approx 2 - 3$. Nevertheless, the high-redshift fraction of GRBs detected with *Swift* will test the validity of SFR5 and SFR6 used to model the GRB data.

The models that fit the data imply that $8 - 12\%$ of *Swift* GRBs occur at $z \gtrsim 5$, in accord with the data as shown in Figure 23. Our model predicts that $2.5 - 6\%$ of GRBs should be detected from $z \geq 7$. If no GRB with $z > 7$ is detected by the time ≈ 100 *Swift* GRBs with measured redshifts are found, then we may conclude that the GRB formation rate has begun to decline above $z \approx 5$. By contrast, if a few $z \gtrsim 7$ GRBs have been detected within the next year or two with *Swift*, then this would be in accord with our model and would support the conjecture of Bromm & Loeb (2006) that a second episode of Population I and II star formation took place at $z \gtrsim 5$, possibly even including some GRBs that originate from Population III stars. Our model parameters suggest that GRBs can be detected with *Swift* to a maximum redshift $z \approx 20$, even given the limits placed on the range of jet angles, in particular, $\theta_{\min} \geq 0.05$.

The relationship between the galaxies that host GRBs and their metallicities remains controversial, with evidence for high-redshift, low-metallicity GRB host galaxies (Fruchter et al. 2006) countered by examples of GRBs found in galaxies with moderate metallicity (Berger et al. 2006; Fynbo et al. 2006a). Stanek et al.

(2006) find that 5 GRBs, or several per cent of the GRB population with known redshifts, are found at low ($z \lesssim 0.25$) redshift in galaxies that have very low metallicity compared with Solar metallicity and with the distribution of metallicities of low-redshift galaxies in the Sloan Digital Sky Survey. In 4 out of the 5 low- z GRBs, the apparent isotropic energy release of these GRBs is much smaller than 10^{51} ergs, and so these GRBs are unrepresentative of typical long duration GRBs. Moreover, the large number of these low redshift GRBs already means that they are not typical of the sample of GRBs considered in this paper, as the model prediction is that $\approx 0.14 - 0.2\%$ of the “classical” GRBs should be detected at low redshifts.⁶ These low-redshift GRBs may also belong to a completely distinct population of GRBs compared to their high-redshift counterparts, as also suggested by the differing luminosity functions of the two populations (Liang et al. 2006). Alternatively, the low-redshift GRBs could be normal GRBs that appear weak because, for example, their jetted emission is observed off-axis (e.g. Yamazaki et al. 2003).

Although we have restricted our treatment to the long-duration, soft-spectrum class of GRBs, the separation between the short hard and long soft class of GRBs is not distinct. Moreover, recent observations of nearby GRBs show that the nearby ($z = 0.125$) GRB 060614, a long duration GRB in terms of its light curve (Gehrels et al. 2006), lacks a supernova excess (Fynbo et al. 2006; Della Valle et al. 2006), does not fit neatly into either the short hard or long soft classes (Zhang 2006), and could represent a separate population of GRBs (Gal-Yam et al. 2006). Phenomenological studies have also indicated that the long GRB population is bimodally distributed in terms of the autocorrelation function of the light curves (e.g., Borgonovo 2004). Tavani (1998) argues for multiple populations by examining the size distributions of different groups of BATSE GRBs separated according to spectral properties. From an analysis of durations of BATSE, Horváth et al. (2006) identifies an intermediate duration population that displays the softest spectra and comprises $\approx 11\%$ of the total BATSE GRBs.

That we were able to obtain good fits to the different data sets using a single GRB model may indicate that the contribution of sub-populations to the total number of GRBs is small. Alternately, the model parameters might have been adjusted to take into account the aggregate long duration GRBs. This can be tested in future work using a larger Swift data set that allows subgroups to be separately studied based on spectra or durations.

Figure 24a shows the model integral size distribution (see eq. [18]) of GRBs predicted by our best fit model. The plots are normalized to the current total number of observed GRBs per year from BATSE, which is 550 bursts per 4π sr exceeding a peak flux of 0.3 photons $\text{cm}^{-2} \text{s}^{-1}$ in the $\Delta E = 50 - 300$ keV band for the $\Delta t = 1.024$ s trigger time (Band 2002). From the model size distribution, we find that ≈ 340 to 360 GRBs per year should be detected with a BATSE-type detector over the full sky above an energy flux threshold of

$\sim 10^{-7}$ ergs $\text{cm}^{-2} \text{s}^{-1}$, or photon number threshold of 0.625 ph $\text{cm}^{-2} \text{s}^{-1}$. This range of values is determined by the two model fits with SFR6 and SFR5, respectively. We estimate from our fits that $\approx 1190 - 1370$ GRBs take place per year per 4π sr with a flux $\gtrsim 10^{-8}$ ergs $\text{cm}^{-2} \text{s}^{-1}$, or 0.0625 ph $\text{cm}^{-2} \text{s}^{-1}$. The field of view of the BAT instrument on Swift is 1.4 sr (Gehrels et al. 2004), implying that Swift should detect $\approx 130 - 150$ GRBs per year; currently, *Swift* observes about 100 GRBs per year. This minor discrepancy may be a consequence of using a flat νF_ν GRB spectrum in our model.

We also show the differential size distribution of BATSE GRBs from the Fourth BATSE catalog (Paciesas et al. 1999) in comparison with our model prediction in Figure 24b. As can be seen, our model gives a good representation of the size distribution of the BATSE GRB distribution within the statistical error bars, except for a slight overprediction of the number of the brightest GRBs (see also Daigne et al. 2006; Böttcher & Dermer 2000). These brightest GRBs typically originate from $z \lesssim 1$, possibly suggesting a slight reduction in the number of GRBs with $z \ll 1$ compared to the GRB rate densities considered. Below a photon number threshold of 0.3 ph $\text{cm}^{-2} \text{s}^{-1}$ in the 50 – 300 keV band, the observed number of GRBs falls rapidly due to the sharp decline in the BATSE trigger efficiency at these photon fluxes (see Paciasas et al. 1999). The size distribution of the *Swift* GRBs will extend to much lower values, ≈ 0.0625 ph $\text{cm}^{-2} \text{s}^{-1}$, and we can use our model to predict the peak flux size distribution to fit the *Swift* data, noting however that the *Swift* triggering criteria are more complicated than a simple rate trigger, particularly near threshold (Band 2006).

We can derive the burst rate $\dot{\rho}$ in our local universe by normalizing our best fit models to the BATSE results of 340 – 360 GRBs per year full sky with peak fluxes exceeding 10^{-7} ergs $\text{cm}^{-2} \text{s}^{-1}$. Comparing this value with the rate calculated from eq. (18) for our best fit models, we obtain local GRB rate densities of $\dot{n}_{\text{GRB}} = 9.6 \text{ Gpc}^{-3} \text{ yr}^{-1}$ for SFR5 and $\dot{n}_{\text{GRB}} = 7.5 \text{ Gpc}^{-3} \text{ yr}^{-1}$ for SFR6. Since the mean volume occupied by an L^* galaxy in the local universe is $\approx 200 \text{ Mpc}^{-3}$ (Loveday et al. 1992; Wijers et al. 1998), we obtain the local event rate in our Galaxy, assumed to be a typical L^* galaxy, to be $\dot{\rho} \approx 1.9 \times 10^{-6}$ and 1.5×10^{-6} events per year per L_* galaxy, for SFR5 and SFR6, respectively. This implies that about 1 event occurs every 0.6 Myrs in our Galaxy. Comparing this to the rate of Type Ib/c supernovae of ≈ 1 every 360 years in our Galaxy (Cappellaro et al. 1999), we estimate that the rate of GRBs is only $\approx 0.06\%$ of the rate of SN Ib/c supernovae in the Galaxy. Berger et al. (2003) find that $\leq 3\%$ of GRBs could originate from SN Ib/c by comparing the radio brightnesses of SN Ib/c with that of SN 1998bw associated with GRB 980425. Our results fall comfortably within the observational limits. We also find that about 1 out of every 20,000 SNe make a GRB, compared to the value of 1 out of every $10^5 - 10^6$ found by Daigne et al. (2006).

If GRBs do occur at the rate of more than once per Myr in the Milky Way, depending on uncertain metallicity effects (Stanek et al. 2006), then the Earth will intercept the beam of a GRB about once every 25 Myrs, given the

⁶ A value of $\approx 0.3\%$ can be estimated by considering the fractional volume within $z = 0.25$ compared with $z \cong 1$, and that the SFR activity at $z \cong 1$ was a factor $\cong 5$ greater than at $z < 0.25$.

beaming factor $\langle f_b^{-1} \rangle \sim 40$ obtained in our analysis. If a Milky Way GRB is located at an average distance of 10 kpc, then the average fluence deposited by the GRB is on the order of $\approx 10^7$ ergs cm^{-2} . Strong astrobiological effects begin to be important when the GRB fluence is $\approx 10^8 - 10^9$ ergs cm^{-2} , or when the GRB occurs within $\approx 1 - 2$ kpc with its beam pointing in our direction (Dermer & Holmes 2005). This will happen perhaps a few times per Gyr, so that GRBs could have significant effects on terrestrial evolution (Melott et al. 2004; Thomas et al. 2005).

The number of jet opening angles measured with follow-up observations of *Swift* GRBs is not yet sufficient to produce a statistically reliable sample. Thus our jet opening angle distribution shown in Figures 20 and 22 with $s = -1.3$ and -1.2 , for SFR5 and SFR6, respectively, provide a prediction for *Swift*. With *Swift* and pre-*Swift* thresholds of $\approx 10^{-8}$ and $\approx 10^{-7}$ ergs $\text{cm}^{-2} \text{ s}^{-1}$, our model predicts the mean measured jet opening angle $\langle \theta_j \rangle \approx 0.16$, and 0.12 rad, respectively, which can be compared with the measured average value of $\langle \theta_j \rangle \approx 0.125$ for the pre-*Swift* sample. Thus we expect to detect more faint low-redshift, large opening angle GRBs that pre-*Swift* satellites could not detect (see also Perna, Sari, & Frail 2003). It is interesting to note that with a better detector sensitivity, the mean jet angle is shifted to a higher angle and not vice versa, as might be expected. This suggests that on average we expect

to see more long-duration bursts with larger opening angle ($\theta_j > 0.12$ radian), meaning that the mean times for the achromatic breaks in the light curves could be longer than for the pre-*Swift* GRBs when one also takes into account the larger mean redshift of the *Swift* sample.

In conclusion, we have developed a physical model for GRBs and obtained parameters to the model by fitting the GRB redshift and opening angle distributions. We could only obtain statistically acceptable joint fits if the comoving rate density of GRBs increases monotonically to $z \gtrsim 5$. Our fitting results give a rate of ≈ 1 GRB every 600,000 yrs in our Galaxy if metallicity effects do not play a large role in the galaxies in which GRBs are formed. In this case, the increase in the GRB rate density to high redshifts would have a different cause, for example, an episode of enhanced star formation at $z \gtrsim 5$ (Bromm & Loeb 2006). The opening angle distribution of GRBs measured with *Swift*, and the fraction of low- z and high- z standard long-duration GRBs will test this model.

We thank D. Band, J. Beacom, E. Berger, J. Bloom, and A. Friedman for discussions and correspondence, and the referee for comments, corrections, and useful suggestions. T. L. is funded through NASA *GLAST* Science Investigation No. DPR-S-1563-Y. The work of C. D. D. is supported by the Office of Naval Research.

APPENDIX

BURSTING RATE OF BEAMED COSMIC SOURCES IN A FLAT Λ CDM UNIVERSE

The differential number of bursts per unit proper time per unit volume with beaming-corrected absolute γ -ray energy release between $\mathcal{E}_{*\gamma}$ and $\mathcal{E}_{*\gamma} + d\mathcal{E}_{*\gamma}$, jet opening cosine angle $\mu_j = \cos \theta_j$ between μ_j and $\mu_j + d\mu_j$, peak energy between ϵ_{pk*} and $\epsilon_{pk*} + d\epsilon_{pk*}$, burst duration between Δt_* and $\Delta t_* + d(\Delta t_*)$, that occur in volume element between V_* and $V_* + dV_*$ within observer angle $\mu = \cos \theta$ between μ and $\mu + d\mu$ during time interval between t_* and $t_* + dt_*$ is given by

$$dN = \dot{n}_*(\alpha, t_*) d\alpha d\mu dV_* dt_* . \quad (\text{A1})$$

Here the parameter α represents the various parameters of the problem, namely $\mathcal{E}_{*\gamma}$, μ_j , ϵ_{pk*} , and Δt_* . Hence, the directional burst rate per unit observer time t is given by

$$\frac{d\dot{N}}{d\Omega} = \frac{\dot{n}_*(\alpha, t_*) d\alpha d\mu dV_*}{d\Omega} \left| \frac{dt_*}{dt} \right| . \quad (\text{A2})$$

In a flat Λ CDM universe, the Robertson-Walker metric describes the line element ds for a homogeneous, isotropic expanding universe, and is given by

$$ds^2 = c^2 dt^2 - R^2(t) \left[\frac{dx^2}{1 - kx^2} + x^2 (d\theta^2 + \sin^2 \theta d\phi^2) \right] , \quad (\text{A3})$$

where $R(t)$ is the dimensionless scale factor of the universe and (x, θ, ϕ) are the *comoving coordinates* of a point at rest in the Hubble flow. The curvature index $k = -1/\mathcal{R}^2$, 0, and $+1/\mathcal{R}^2$ represents an open, flat, and closed universe model, respectively, where \mathcal{R} is the radius of curvature at the present epoch. At the present epoch, we let $R(t) = 1$ and x correspond to the physical distance between two comoving points. The ratio of the scale factor, $R(t_*)$, at the emitted time, t_* , to the scale factor $R = R(t_0)$, at the present time, t_0 , is given by,

$$\frac{R_*}{R} = \frac{1}{1+z} = \frac{\lambda_*}{\lambda} .$$

The following relations hold from the above definition, namely

$$1+z = \frac{\nu_*}{\nu} = \frac{\Delta t}{\Delta t_*} = \frac{\epsilon_*}{\epsilon} , \quad (\text{A4})$$

where the last expression applies to photons and relativistic particles in an expanding universe with $R_* = R(t_*)$, and $R = R(t_0)$.

To calculate the differential volume element dV_* in equation (A2), we utilize the fact that the product of differential length elements corresponding to infinitesimal changes in the coordinates x , θ , and ϕ equals the differential volume element dV . Hence, the proper volume element of a slice of the universe at time t_* is, from eq. (A3),

$$dV_* = \frac{(R_*x)^2 R_* dx d\Omega_*}{\sqrt{1 - kx^2}} \xrightarrow{k \rightarrow 0} R_*^3 x^2 dx d\Omega_* , \quad (\text{A5})$$

specializing to a flat universe, where $d\Omega_*$ represents the solid angle at the emitted time. Substituting equation (A5) into equation (A2) for dV_* , we obtain

$$\frac{d\dot{N}}{d\Omega} = \dot{n}_*(\alpha, t_*) R_*^3 x^2 dx d\alpha d\mu \left| \frac{dt_*}{dt} \right| , \quad (\text{A6})$$

where in a homogeneous isotropic expanding universe with no intervening gravitating matter to distort the paths of the light rays, $d\Omega_* = d\Omega$.

Light travels along a null geodesic, $ds = 0$, which is a path along which θ and ϕ are constants. Thus in the Robertson-Walker metric the proper time element elapsed for a photon to propagate a differential comoving distance at earlier time t_* is just $cdt_* = R_* dx$ or $dx = cdt_*/R_*$. Upon substituting dx into equation (A6) we obtain,

$$\frac{d\dot{N}}{d\Omega} = \frac{c \dot{n}_*(\alpha, z) (R_*x)^2 d\alpha d\mu}{1+z} \left| \frac{dt_*}{dz} \right| dz , \quad (\text{A7})$$

where we have also expressed everything in terms of redshift z by transforming from the variable t_* to z .

An expression for $(R_*x)^2$ is derived by recalling the relationship between energy flux Φ_E and luminosity distance d_L , namely,

$$\begin{aligned} \frac{d\mathcal{E}}{dAdt} = \Phi_E &= \frac{L_*}{4\pi d_L^2} = \frac{d\mathcal{E}_*}{4\pi d_L^2 dt_*} = (4\pi d_L^2)^{-1} \left(\frac{d\mathcal{E}_*}{d\mathcal{E}} \right) \left(\frac{dt}{dt_*} \right) \left(\frac{d\mathcal{E}}{dAdt} \right) dA \\ &= \frac{(1+z)^2}{4\pi d_L^2} \Phi_E dA , \end{aligned}$$

or

$$\frac{(1+z)^2}{4\pi d_L^2} dA = 1 , \quad (\text{A8})$$

where the area element dA of the Robertson-Walker metric is

$$dA = (Rx)^2 \sin\theta \, d\theta d\phi = R^2 x^2 d\Omega .$$

Hence

$$\frac{dA_*}{dA} = \left(\frac{R_*x}{Rx} \right)^2 \frac{d\Omega_*}{d\Omega} = \frac{1}{(1+z)^2} , \quad (\text{A9})$$

where we have utilized equation (A4) and use $d\Omega_* = d\Omega$. Substituting equation (A9) into equation (A8) for dA , we obtain

$$(R_*x)^2 = \frac{d_L^2}{(1+z)^4} . \quad (\text{A10})$$

For a flat Λ CDM universe (Peebles 1993),

$$\left| \frac{dz}{dt_*} \right| = H_0 (1+z) \sqrt{\Omega_m (1+z)^3 + \Omega_\Lambda} , \quad (\text{A11})$$

where Ω_m and Ω_Λ are the ratios of the energy densities of total mass, dominated by dark matter, and dark energy, respectively, compared to the critical density. Substituting equations (A10) and (A11) into equation (A7) gives

$$\frac{d\dot{N}}{d\Omega} = \frac{c}{H_0} \frac{d_L^2(z) \dot{n}_*(\alpha, z) d\alpha d\mu dz}{(1+z)^6 \sqrt{\Omega_m (1+z)^3 + \Omega_\Lambda}} , \quad (\text{A12})$$

for randomly oriented GRB sources. After using the relation that the proper density $\dot{n}_*(\alpha, z)$ increases with redshift $\propto (1+z)^3$ in the comoving density $\dot{n}_{co}(\alpha, z)$, that is $\dot{n}_*(\alpha, z) = (1+z)^3 \dot{n}_{co}(\alpha, z)$, we obtain the result given in equation (8).

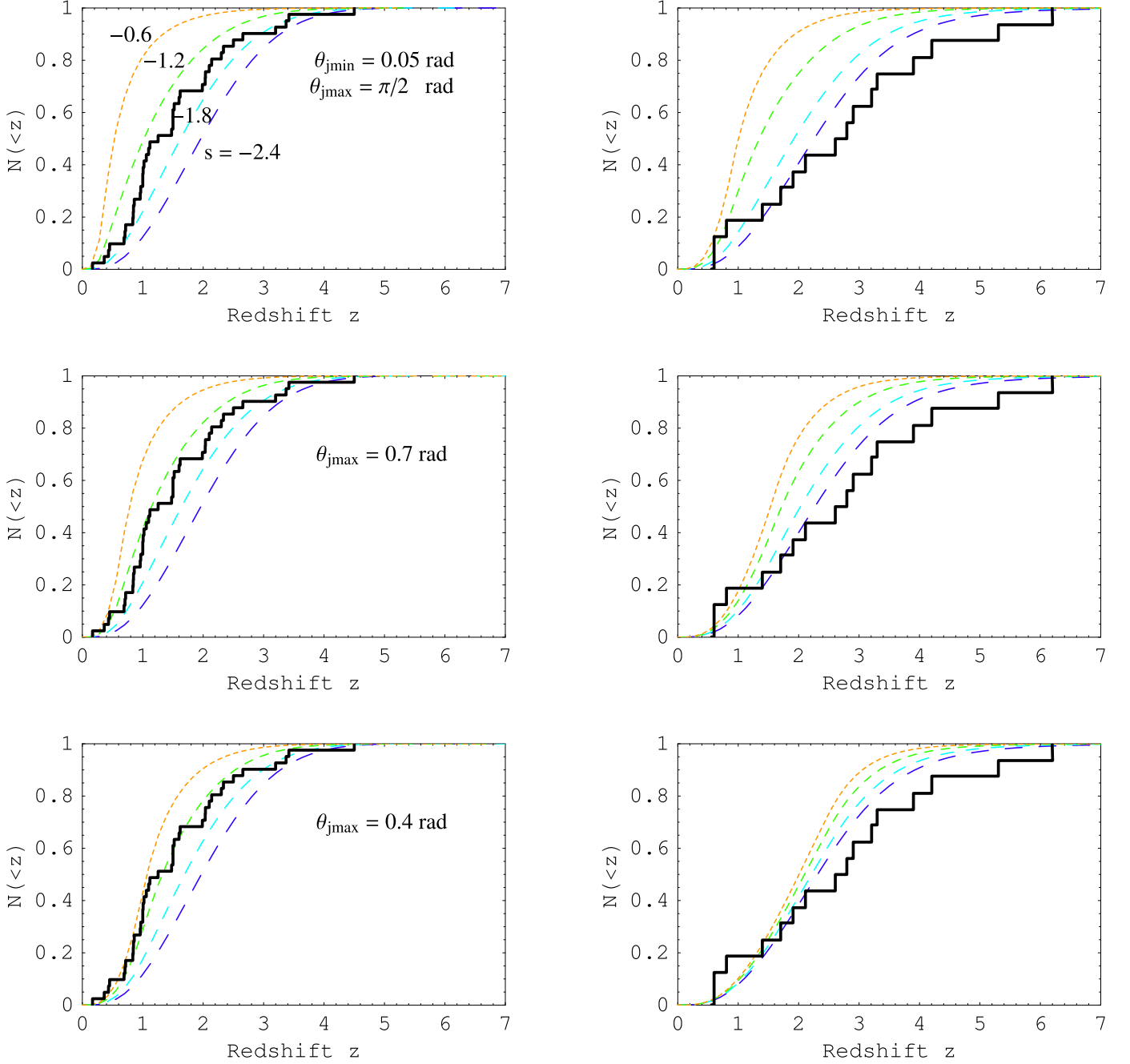


FIG. 9.— Measured and model redshift distributions for SFR3 (Hopkins & Beacom 2006). In the left column, from top to bottom, we have the pre-*Swift* cumulative redshift distribution with the assumed range of jet opening angles $\theta_{\text{jmin}} = 0.05$, $\theta_{\text{jmax}} = \pi/2$, 0.7, and 0.4 radians, respectively. The right column has results as in the left column but for *Swift* data. In each panel, each curve represents the cumulative redshift distribution for different jet opening angle power-law indices s , where $s = -0.6$, -1.2 , -1.8 , and -2.4 , from far left to far right, respectively. The assumed gamma-ray energy is $\mathcal{E}_{*\gamma} = 2 \times 10^{51}$ ergs.

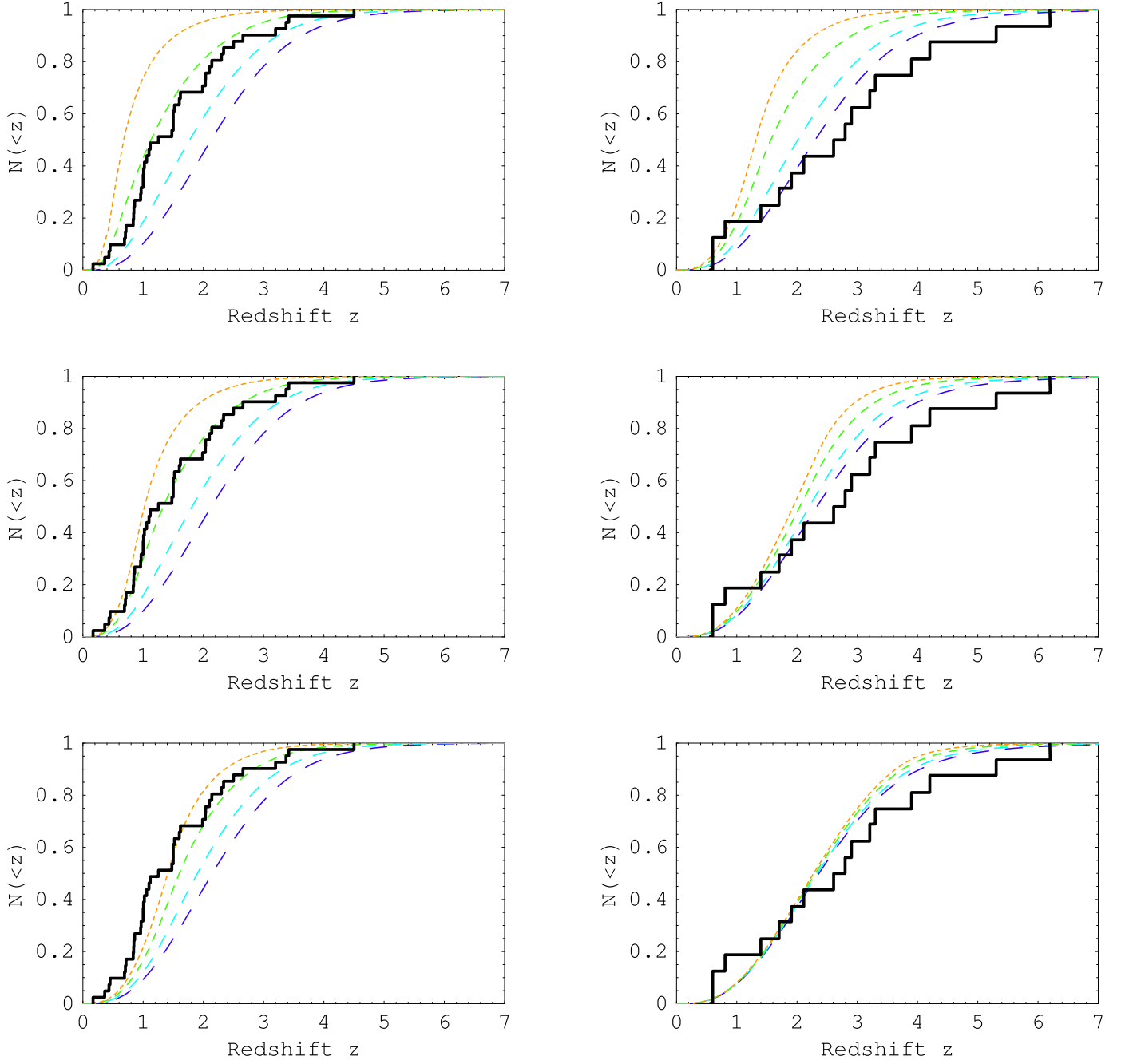


FIG. 10.— SFR3: Same as Figure 9 but for $\mathcal{E}_{*\gamma} = 5 \times 10^{51}$ ergs.

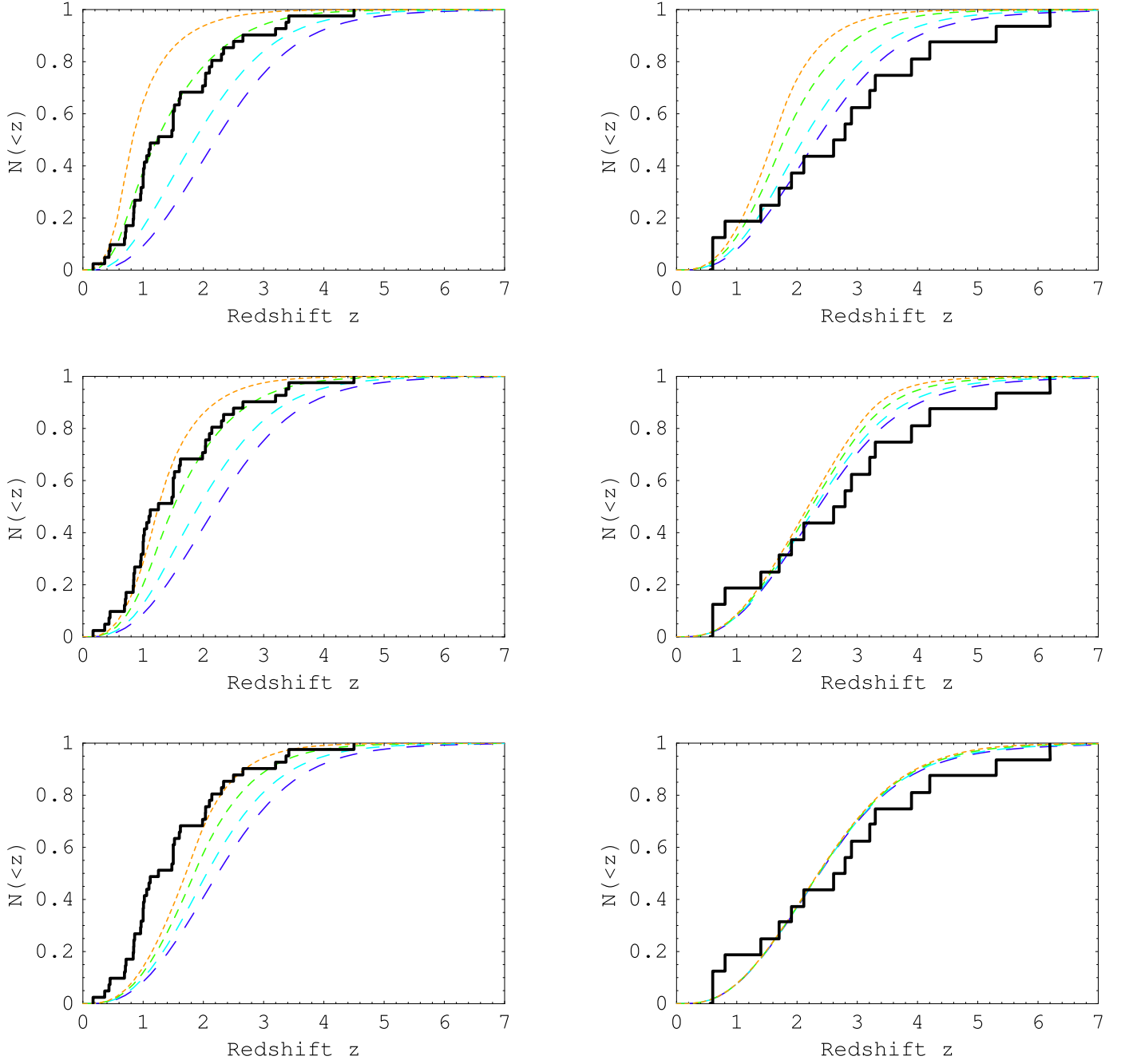


FIG. 11.— SFR3: Same as Figure 9 but for $\mathcal{E}_{*\gamma} = 10^{52}$ ergs.

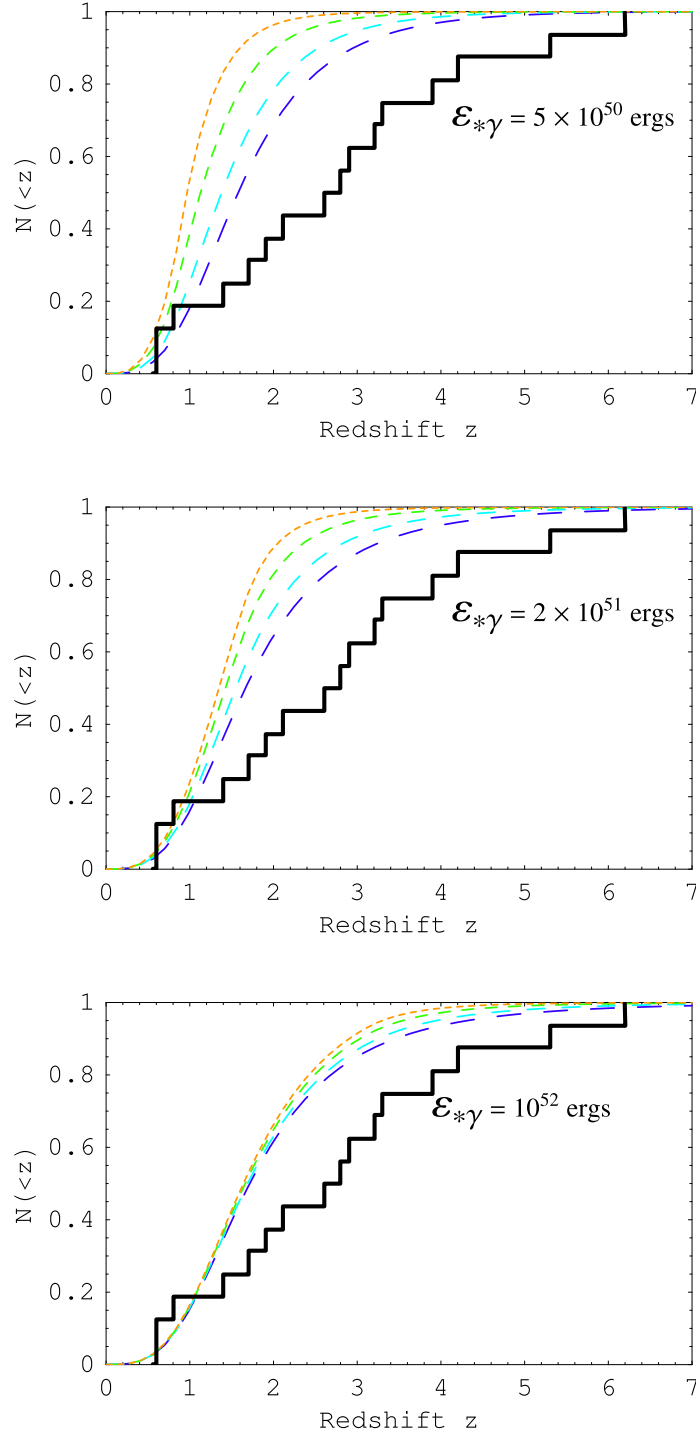


FIG. 12.— SFR2: *Swift* cumulative redshift distribution with an assumed range of the jet opening angles $\theta_{\text{jmin}} = 0.05$ and $\theta_{\text{jmax}} = 0.7$ radians. From top to bottom, the assumed gamma-ray energies are 5×10^{50} , 2×10^{51} , and 10^{52} ergs, respectively. Each curve represents the cumulative redshift distribution for different power-law indices s , where $s = -0.6, -1.2, -1.8,$ and -2.4 , from far left to far right, respectively.

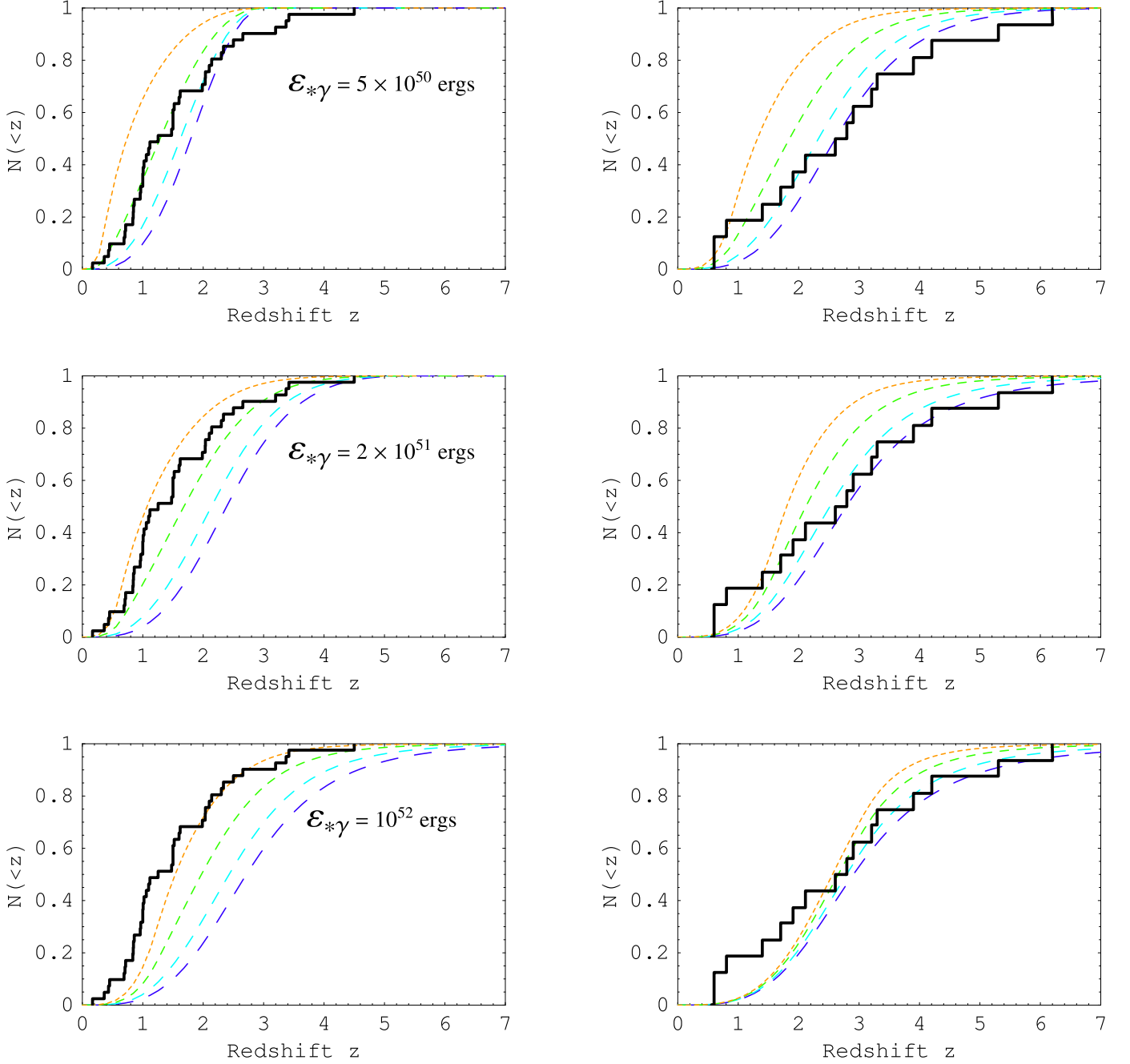


FIG. 13.— SFR4: In the left column from top to bottom, we have the pre-*Swift* cumulative redshift distribution with the assumed gamma-ray energy $\mathcal{E}_{*\gamma} = 5 \times 10^{50}$, 2×10^{51} , and 10^{52} ergs, and an assumed range of the jet opening angles between $\theta_{j\min} = 0.05$ and $\theta_{j\max} = 0.7$ radians. The left and right columns show the model distributions for pre-*Swift* and *Swift* data, respectively. In each panel, each curve represents the cumulative redshift distribution for different indices s , where $s = -0.6, -1.2, -1.8,$ and -2.4 , from far left to far right, respectively.

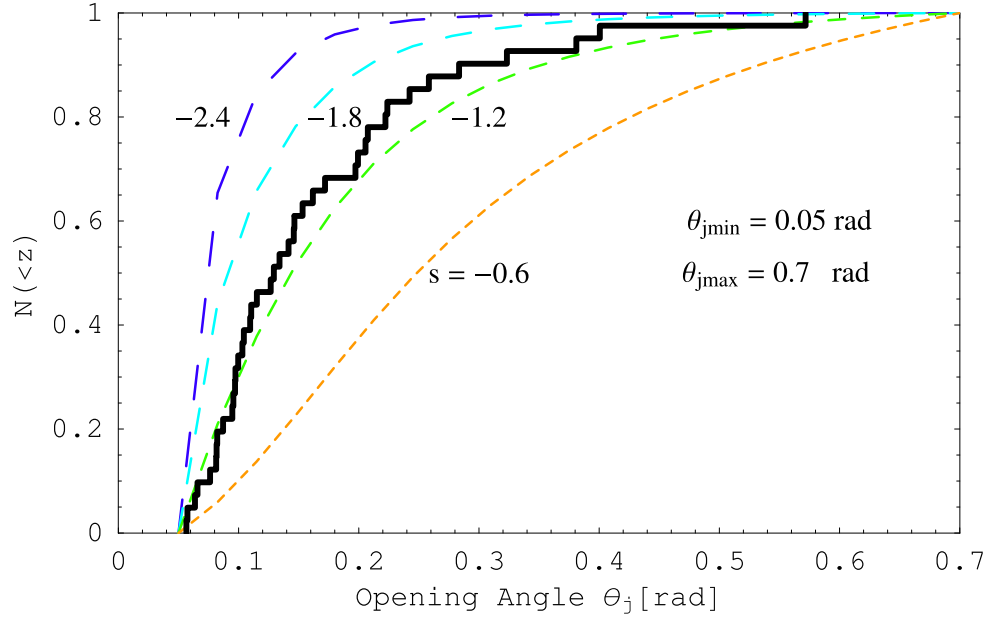


FIG. 14.— SFR4: pre-*Swift* cumulative opening-angle distribution with an $\mathcal{E}_{* \gamma} = 10^{52}$ ergs, and an assumed range of the jet opening angles between $\theta_{j \min} = 0.05$ and $\theta_{j \max} = 0.7$ radians. Each curve represents the cumulative opening-angle distribution for different indices s , where $s = -0.6, -1.2, -1.8,$ and -2.4 , from far right to far left, respectively.

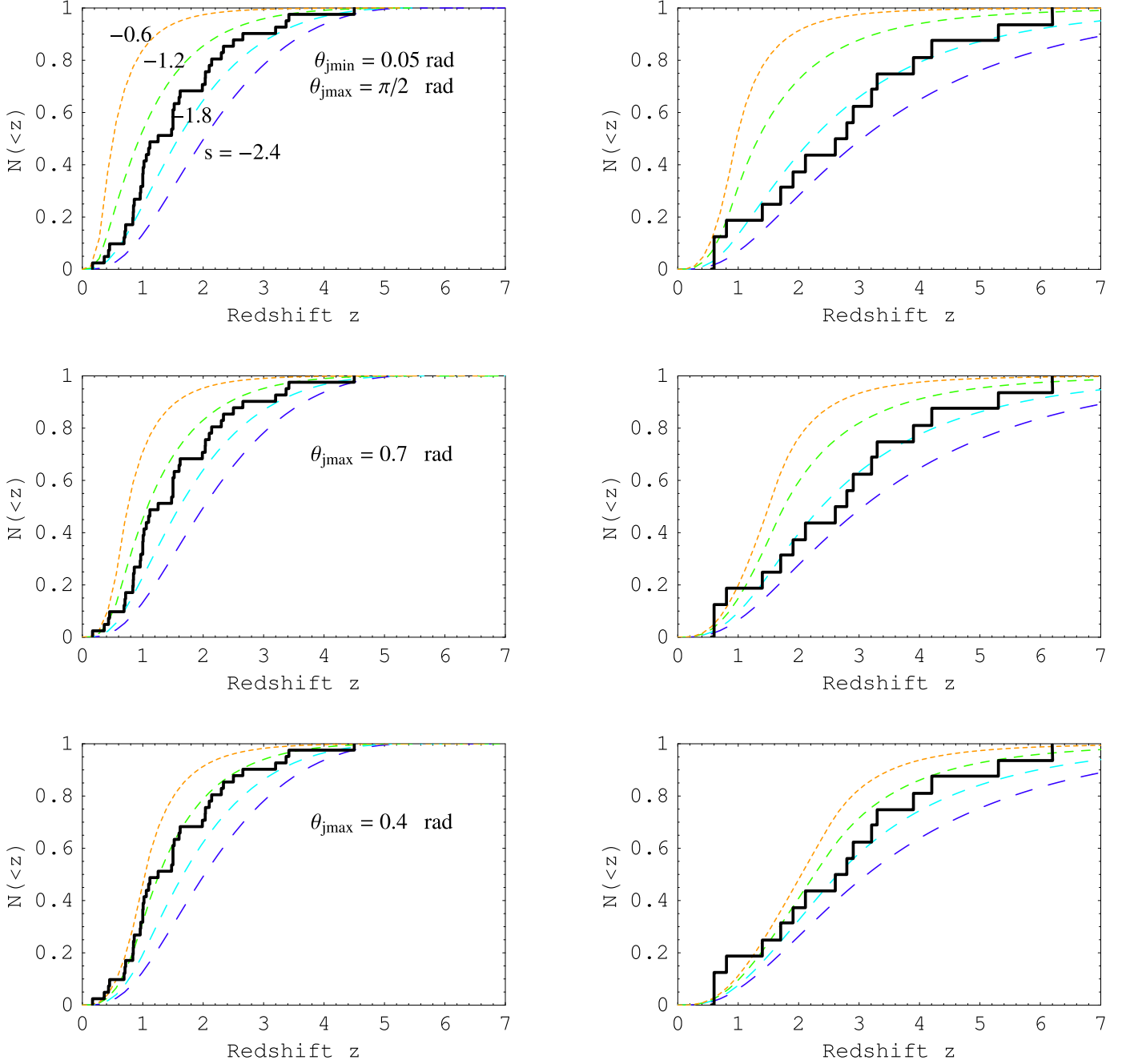


FIG. 15.— SFR5: In the left column, from top to bottom, we have the pre-*Swift* cumulative redshift distribution with the jet opening angles ranging from $\theta_{j\min} = 0.05$ to $\theta_{j\max} = \pi/2$, 0.7, and 0.4 radians, respectively. In the right column we have the same thing as in the left column but for *Swift* data. In each panel, each curve represents the cumulative redshift distribution for indices s , where $s = -0.6$, -1.2 , -1.8 , and -2.4 , from far left to far right, respectively. The assumed gamma-ray energy is $\mathcal{E}_{*\gamma} = 2 \times 10^{51}$ ergs.

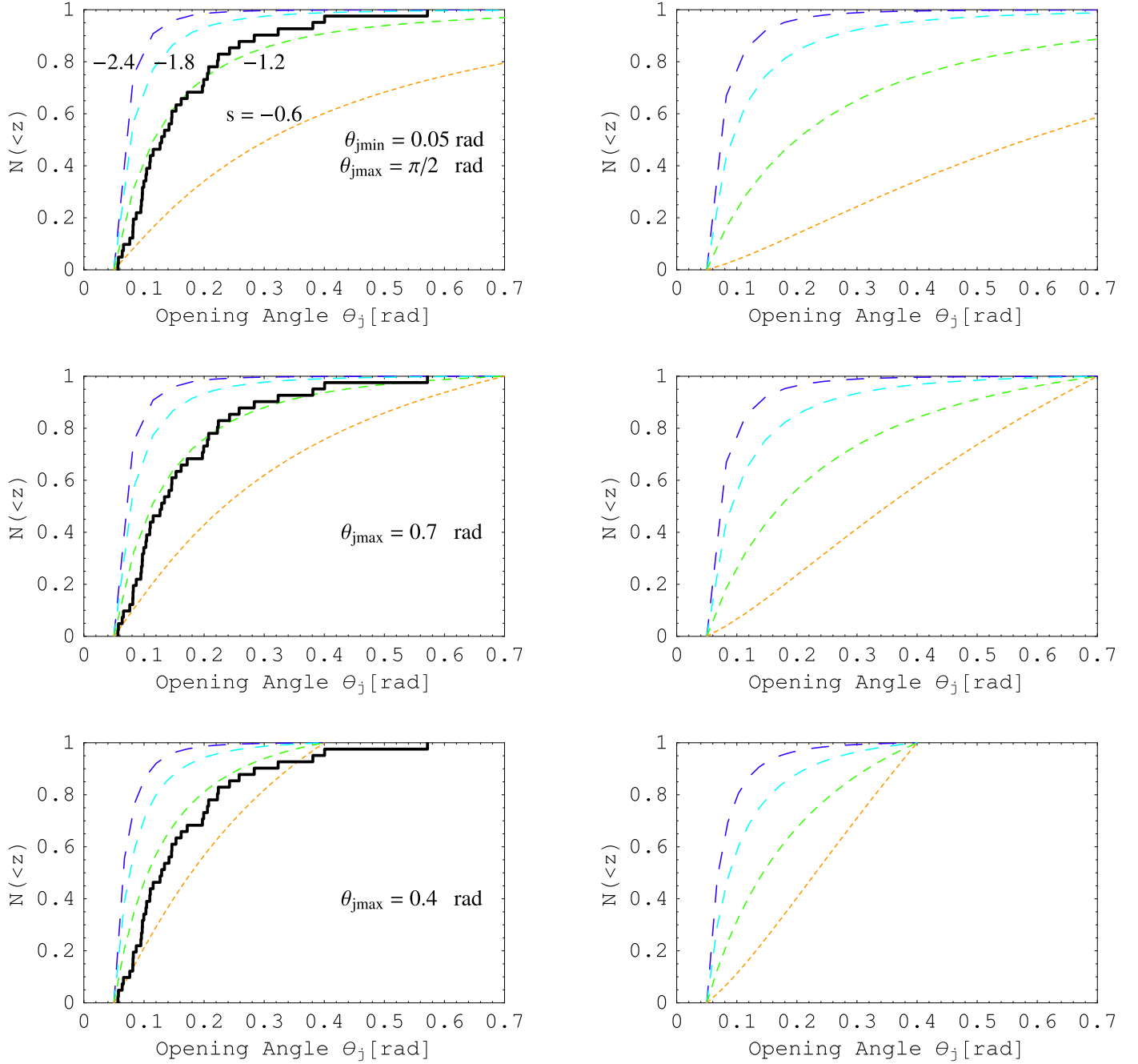


FIG. 16.— SFR5: In the left column from top to bottom, we have the pre-*Swift* cumulative opening-angle distribution with the jet opening angles ranging from $\theta_{j\min} = 0.05$ to $\theta_{j\max} = \pi/2$, 0.7, and 0.4 radians, respectively. In the right column we have the same thing as in the left column but for the *Swift* data. In each panel, each curve represents the cumulative redshift distribution for indices $s = -0.6$, -1.2 , -1.8 , and -2.4 , from far right to far left, respectively. The assumed gamma-ray energy is $\mathcal{E}_{*\gamma} = 2 \times 10^{51}$ ergs.

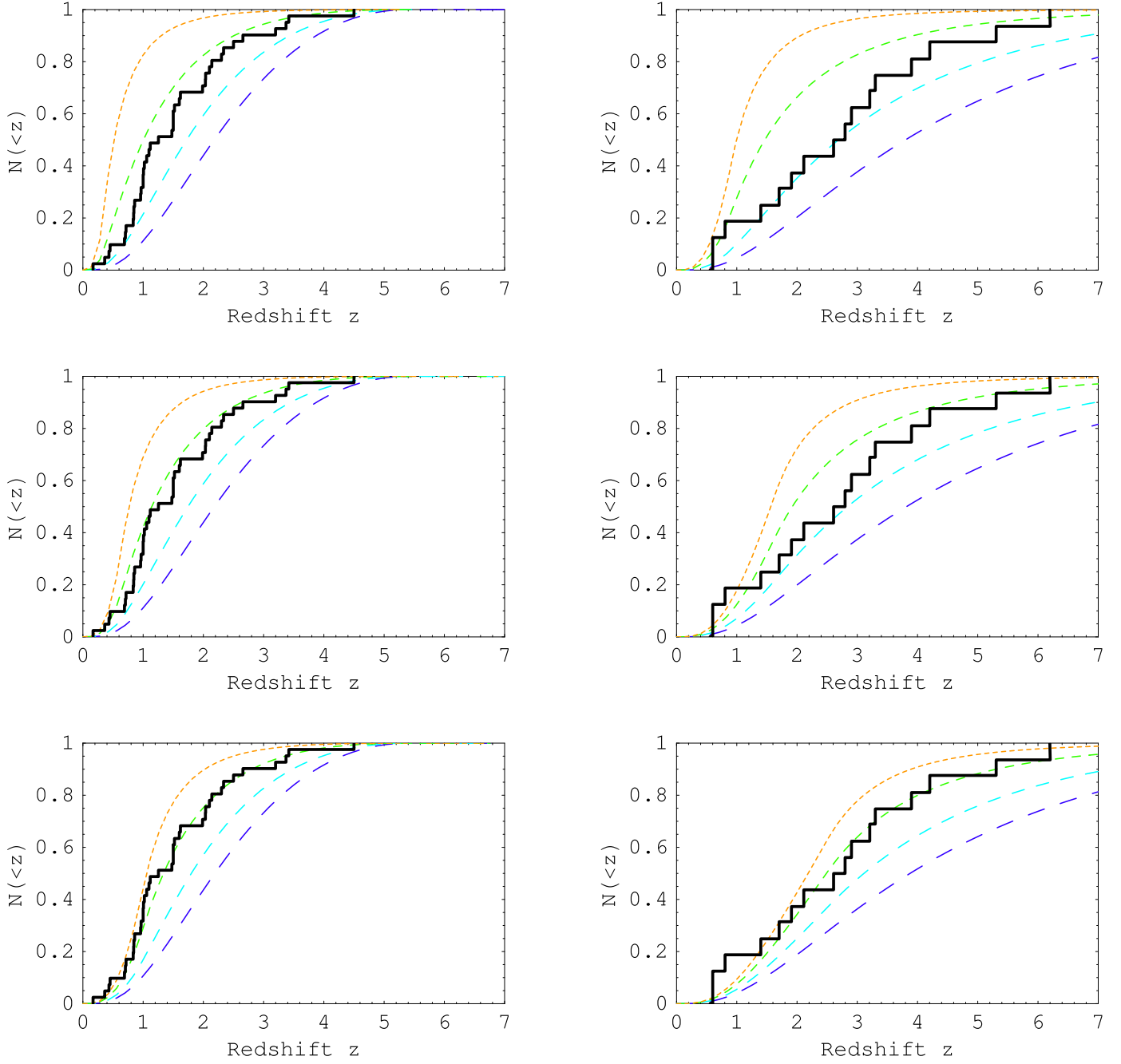


FIG. 17.— SFR6: Same as Figure 15 with $\mathcal{E}_{*\gamma} = 2 \times 10^{51}$ ergs.

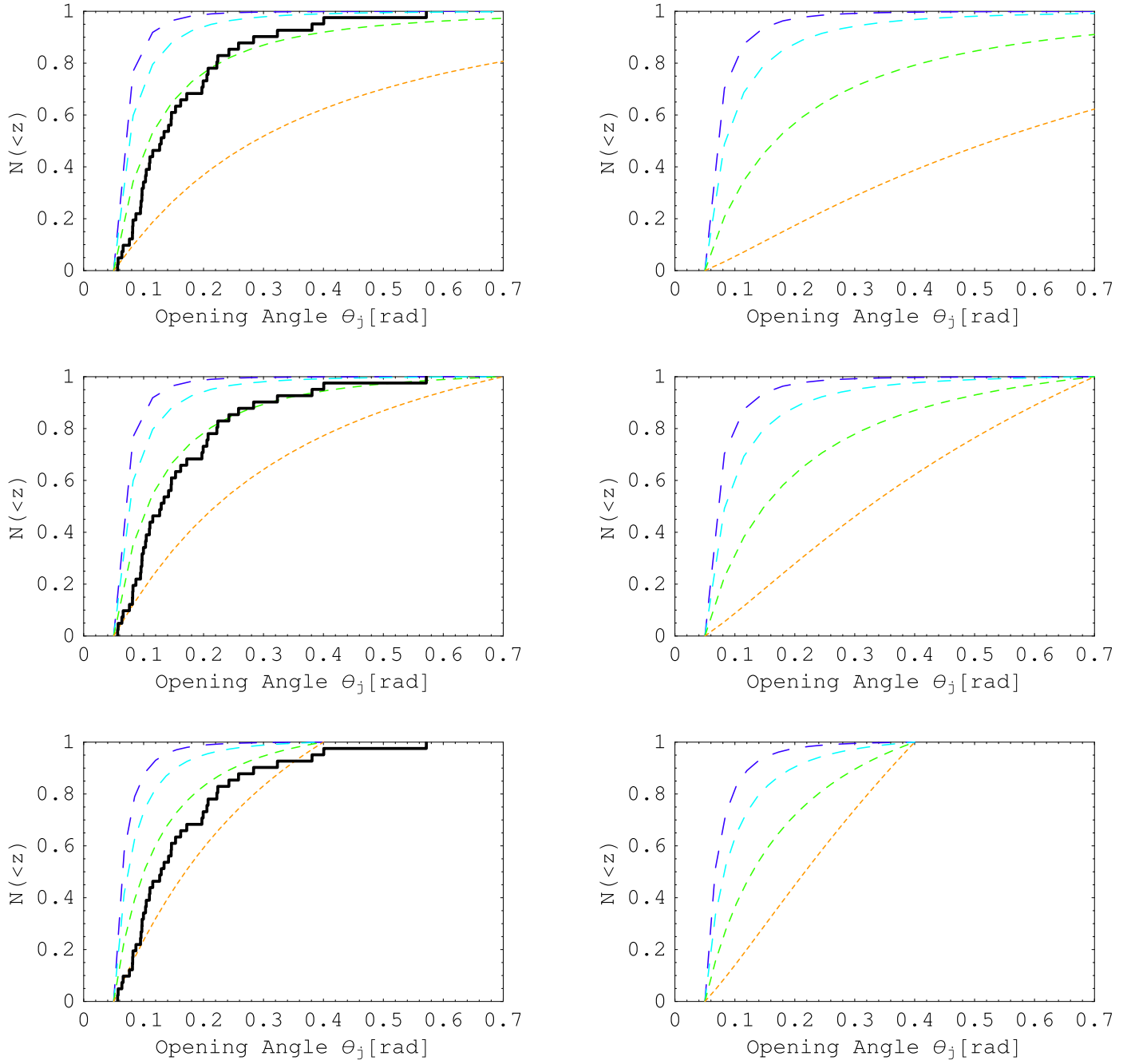


FIG. 18.— SFR6: Same as Figure 16 with $\mathcal{E}_{* \gamma} = 2 \times 10^{51}$ ergs.

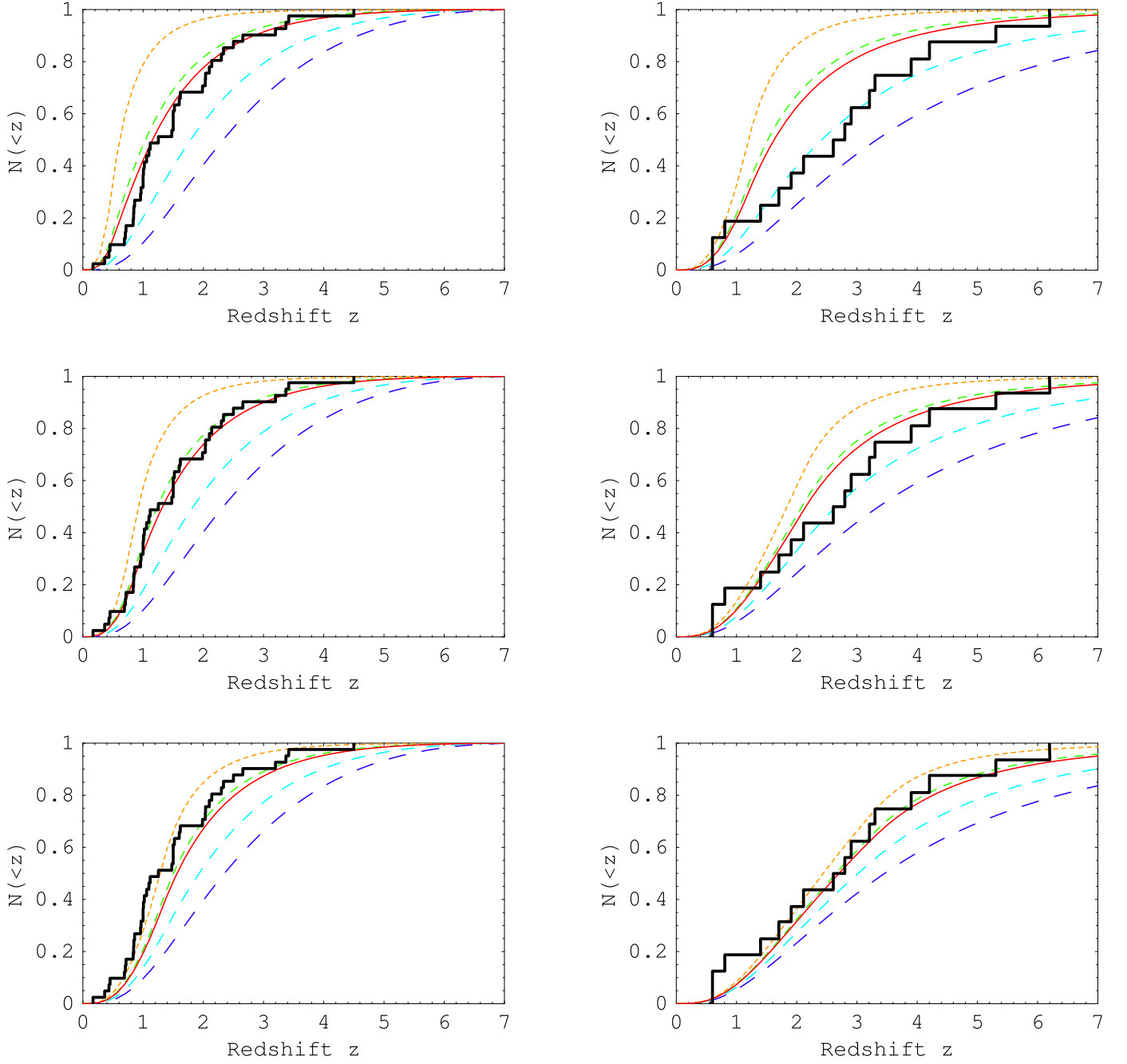


FIG. 19.— SFR5: Same as Figure 15 with $\mathcal{E}_{*\gamma} = 4 \times 10^{51}$ ergs. The solid curves are for $s = -1.3$.

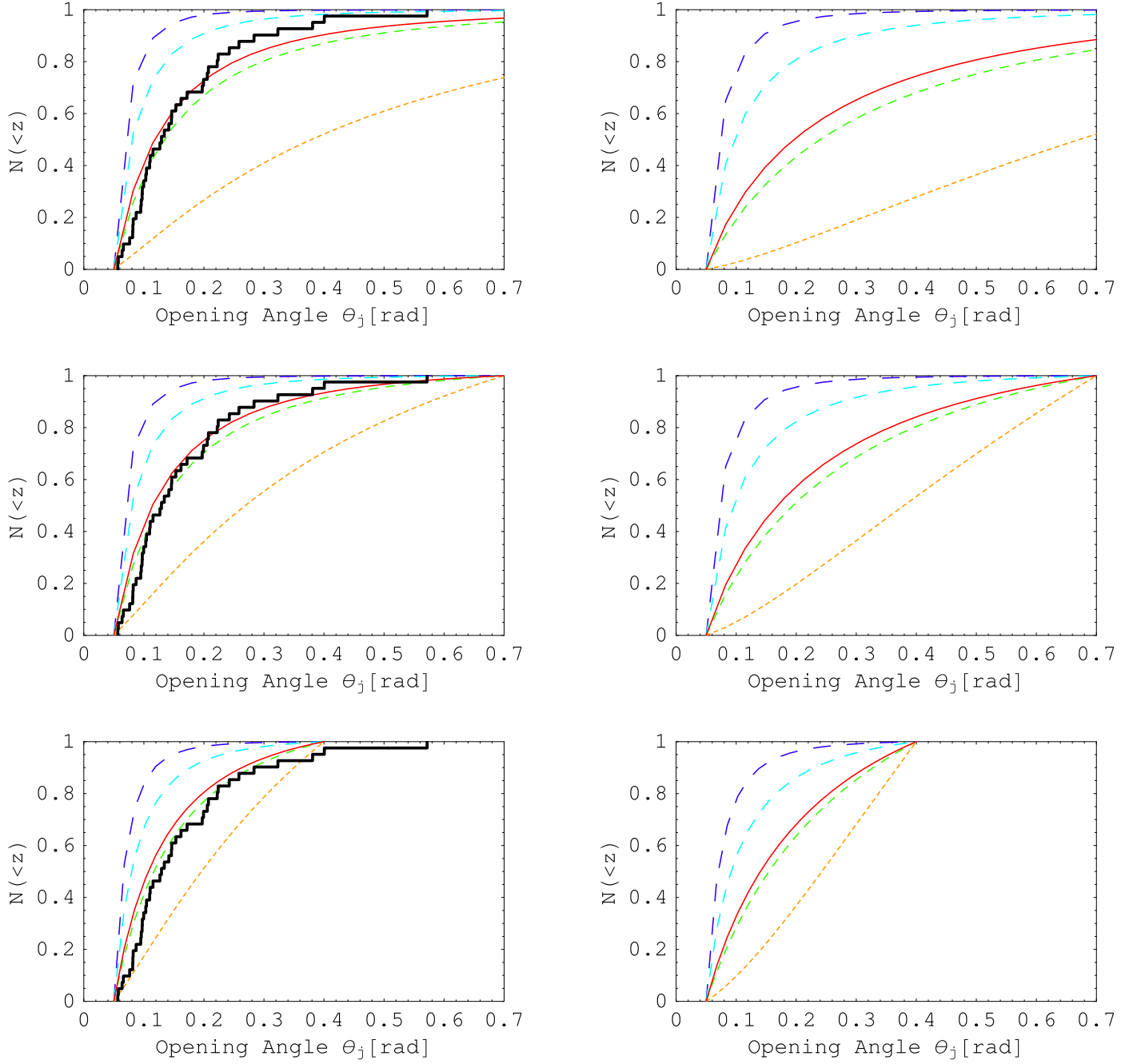


FIG. 20.— SFR5: Same as Figure 16 with $\mathcal{E}_{s\gamma} = 4 \times 10^{51}$ ergs. The solid curves are for $s = -1.3$.

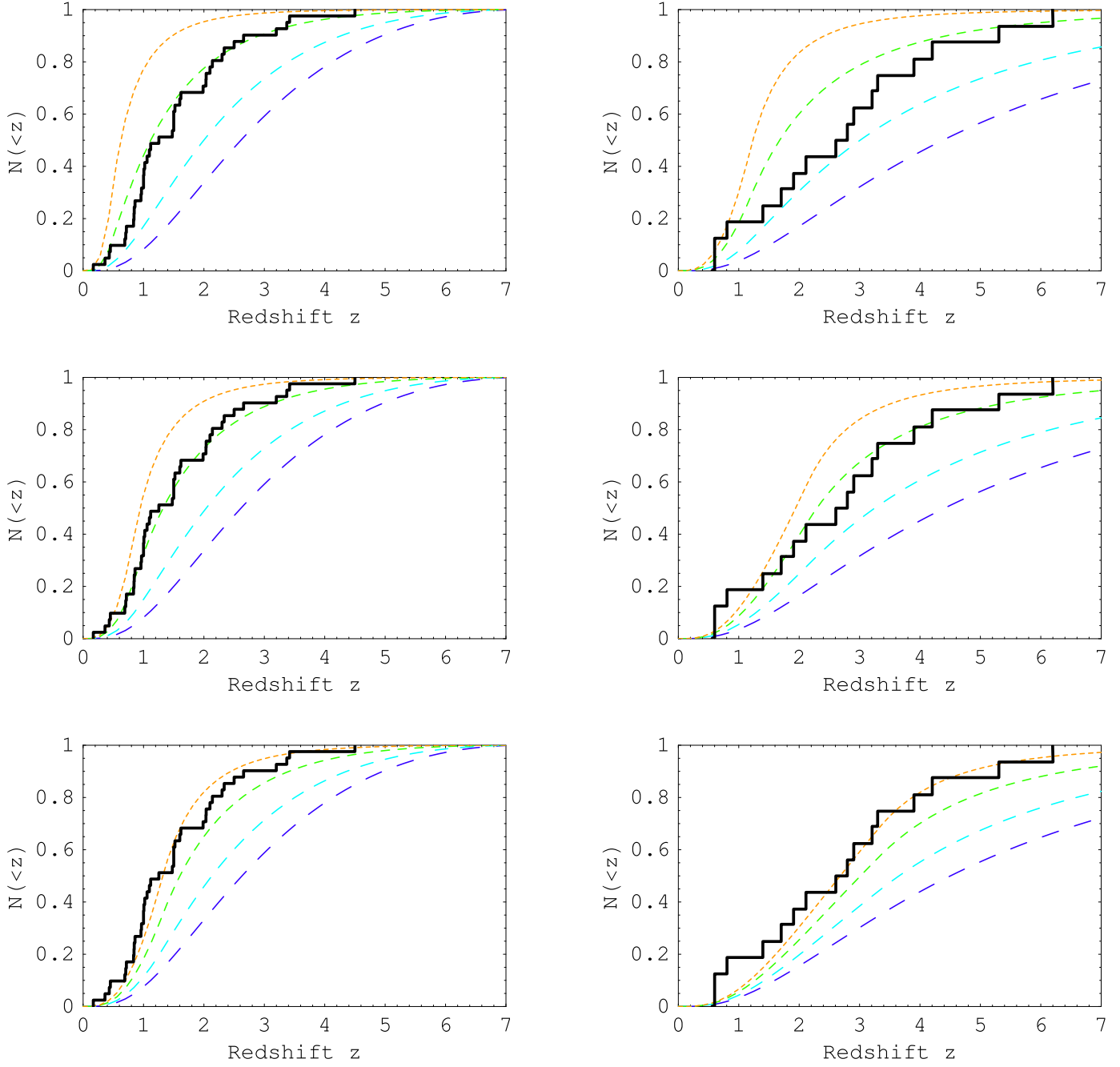


FIG. 21.— SFR6: Same as Figure 15 with $\mathcal{E}_{*\gamma} = 4 \times 10^{51}$ ergs.

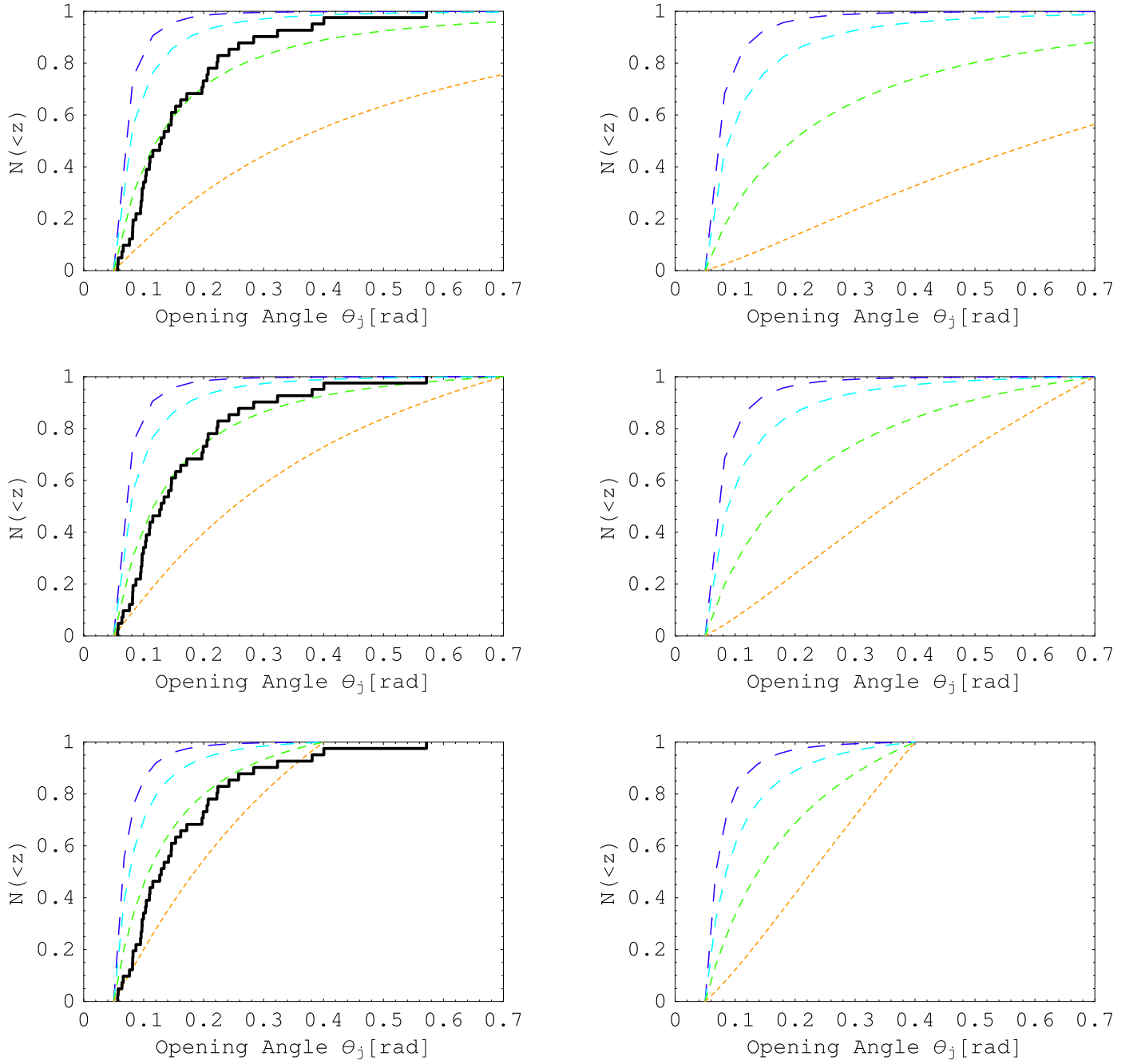


FIG. 22.— SFR6: Same as Figure 16 with $\mathcal{E}_{* \gamma} = 4 \times 10^{51}$ ergs.

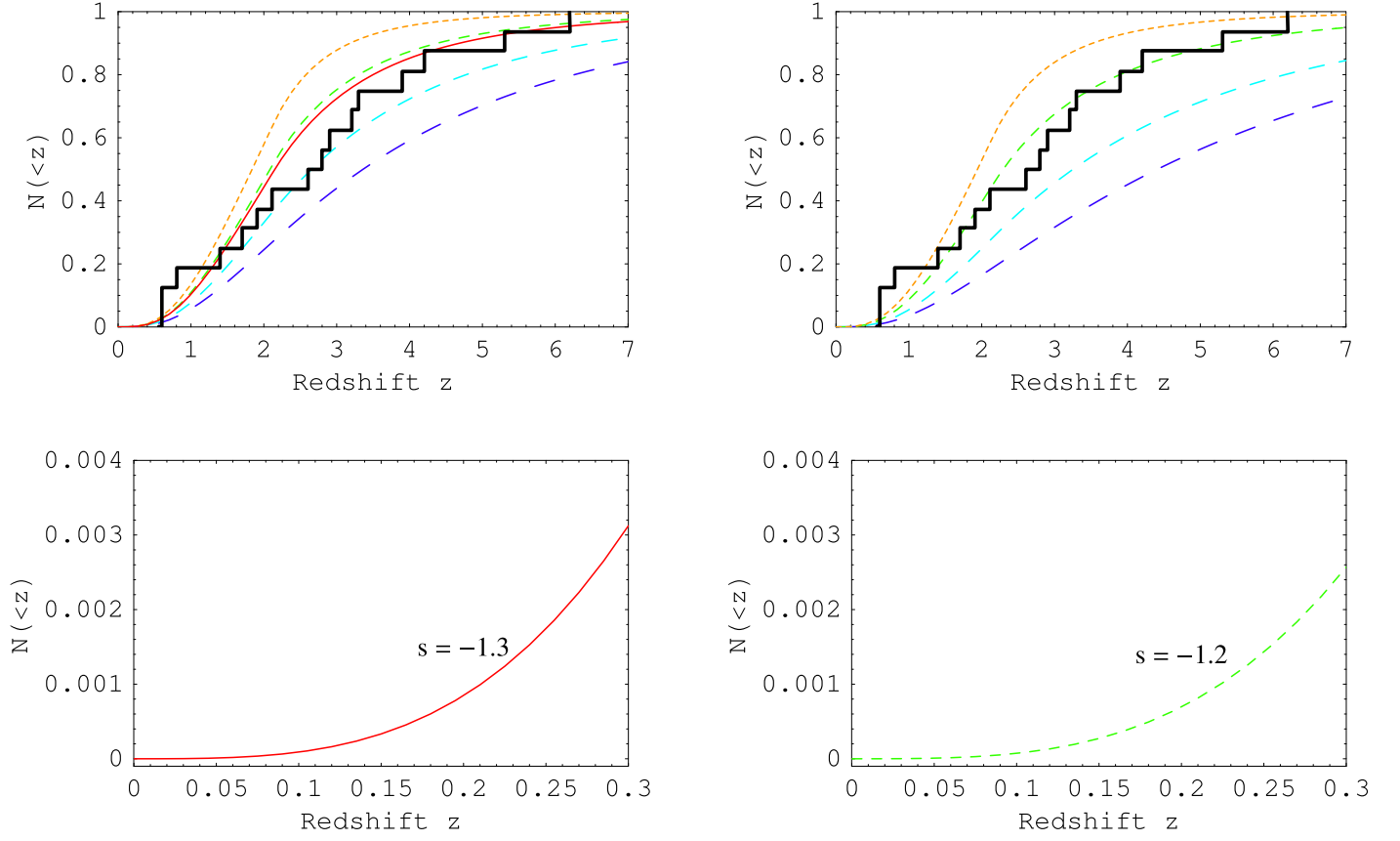


FIG. 23.— *Swift* cumulative redshift distribution assuming SFR5 (left column) and SFR6 (right column), with $\mathcal{E}_{*\gamma} = 4 \times 10^{51}$ ergs. The two bottom panels show the above best-fitted results at $z \leq 1$ in more detail.

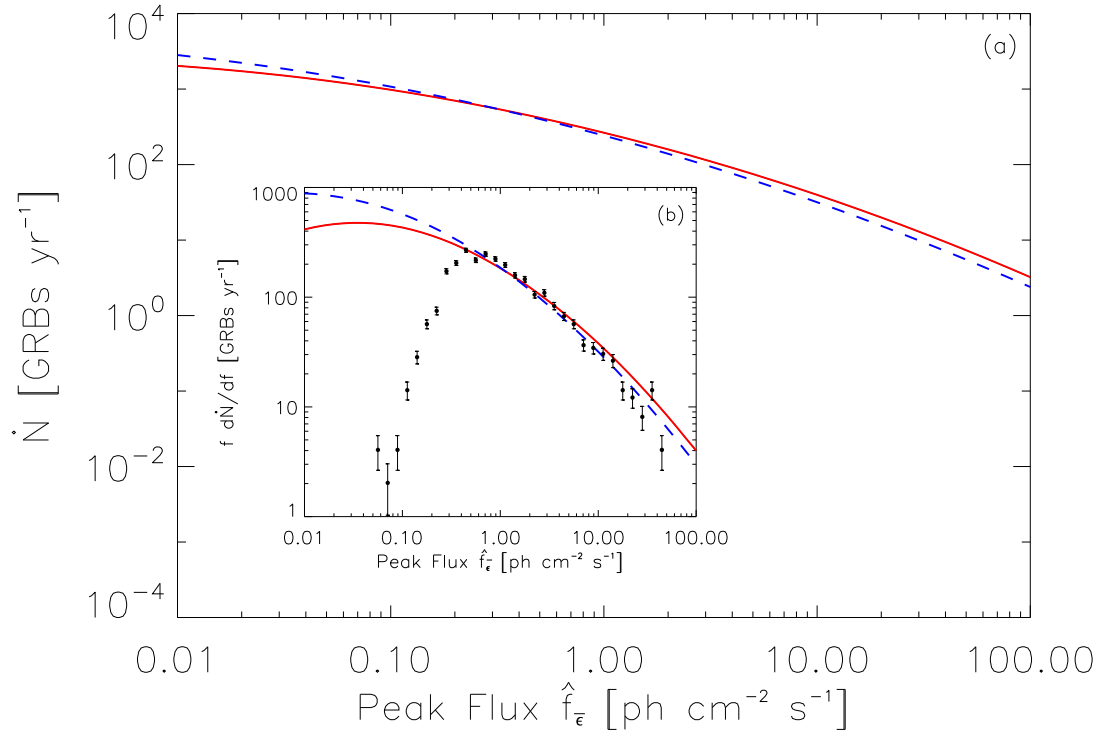


FIG. 24.— Integral size distributions (a) for SFR5 (solid) and SFR6 (dash curve), respectively. The inset is the differential size distributions (b) for SFR5 (solid) and SFR6 (dash curve), respectively. The filled circles curve represents the 1024 ms trigger timescale from the 4B catalog data, containing 1292 bursts.

REFERENCES

- Amati, L., et al. 2002, *A&A*, 390, 81
 Bagoly, Z., et al. 2006, *A&A*, 453, 797
 Band, D. L. 2002, *ApJ*, 578, 806
 Band, D. L. 2003, *ApJ*, 588, 945
 Band, D. L. 2006, *ApJ*, 644, 378
 Barthelmy, S. D., et al. 2005, *Nature*, 438, 994
 Berger, E., Fox, D. B., Kulkarni, S. R., Frail, D. A., & Djorgovski, S. G. 2006, *ApJ*, submitted (astro-ph/0609170)
 Berger, E., Kulkarni, S. R., Frail, D. A., & Soderberg, A. M. 2003, *ApJ*, 599, 408
 Berger, E. et al. 2005, *ApJ*, 634, 501
 Blain, A. W., & Natarajan, P. 2000, *ApJ*, 312, L35
 Blain, A. W. et al. 1999, *MNRAS*, 309, 715
 Bloom, J. S., Frail, D. A., & Kulkarni, S. R. 2003, *ApJ*, 594, 674
 Borgonovo, L. 2004, *A&A*, 418, 487
 Böttcher, M., & Dermer, C. D. 2000, *ApJ*, 529, 635
 Bromm, V., & Loeb, A. 2002, *ApJ*, 575, 111
 Bromm, V., & Loeb, A. 2006, *ApJ*, 642, 382
 Cappellaro, E., Evans, R., & Turatto, M. 1999, *A&A*, 351, 459
 Ciardi, B., & Loeb, A. 2000, *ApJ*, 540, 687
 Daigne, F., Rossi, E., & Mochkovitch, R. 2006, *MNRAS*, 372, 1034
 DellaValle, M., et al. 2006, *Nature*, 444, 1050
 Dermer, C. D. 1992, *Phys. Rev. Lett.*, 68, 1799
 Dermer, C. D. 2006, *ApJ*, in press (astro-ph/0605402)
 Dermer, C. D., & Holmes, J. M. 2005, *ApJ*, 628, L21
 Frail, D. A. et al. 2001, *ApJ*, 562, L55
 Friedman, A. S., & Bloom, J. S. 2005, *ApJ*, 627, 1
 Fruchter, A. S., et al. 2006, *Nature*, 441, 463
 Fynbo, J. P. U., et al. 2006, *Nature*, 444, 1047
 Fynbo, J. P. U., et al. 2006a, *A&A*, 451, L47
 Gal-Yam et al., 2006, *Nature*, 444, 1053
 Gehrels, N. et al. 2004, *ApJ*, 611, 1005
 Gehrels, N. et al. 2006, *Nature*, 444, 1044
 Ghirlanda, G. et al. 2004, *ApJ*, 613, L13
 Guetta, D., Piran, T., & Waxman, E. 2005, *ApJ*, 619, 412
 Hopkins, A. M., & Beacom, J. F. 2006, *ApJ*, 651, 142
 Horváth, I., Balázs, L. G., Bagoly, Z., Ryde, F., & Mészáros, A. 2006, *A&A*, 447, 23
 Jakobsson, P. et al. 2006, *A&A*, 447, 897
 Lamb, D. Q., & Reichart, D. E. 2000, *ApJ*, 536, 1
 Liang, E., Zhang, B., Virgili, F., & Dai, Z. G. 2006, *ApJ*, submitted (astro-ph/0605200)
 Lloyd-Ronning, N. M., Fryer, C. L., & Ramirez-Ruiz, E. 2002, *ApJ*, 574, 554
 Loveday, J., Peterson, B. A., Efstathiou, G., & Maddox, S. J. 1992, *ApJ*, 390, 338
 Melott, A. L., et al. 2004, *International Journal of Astrobiology*, 3, 55
 Mészáros, A., Bagoly, Z., Balázs, L. G., & Horvath, I., 2006, *A&A*, 455 785
 Mészáros, A., & Mészáros, P. 1996, *ApJ*, 466, 29
 Mészáros, P. 2006, *Reports of Progress in Physics*, 69, 2259
 Mészáros, P., & Rees, M. J. 1997, *ApJ*, 482, L29
 Mészáros, P., Rees, M. J., & Wijers, R. A. M. J. 1998, *ApJ*, 499, 301
 Mortsell, E., & Sollerman, J. 2005, *JCAP*, 6, 9
 Natarajan, P., Albanna, B., Hjorth, J., Ramirez-Ruiz, E., Tanvir, N., & Wijers, R. 2005, *MNRAS*, 364, L8
 Paciesas, W. S., et al. 1999, *ApJS*, 122, 465
 Panaitescu, A., & Kumar, P. 2001, *ApJ*, 560, L49
 Peebles, P. J. E. 1993, *Princeton Series in Physics*, Princeton, NJ: Princeton University Press
 Perna, R., Sari, R., & Frail, D. 2003, *ApJ*, 594, 379
 Porciani, C., & Madau, P. 2001, *ApJ*, 548, 522
 Rossi, E., Lazzati, D., & Rees, M. J. 2002, *ApJ*, 332, 945
 Schmidt, M. 1999, *ApJ*, 523, L117
 Spergel, D. N., et al. 2003, *ApJS*, 148, 175
 Stanek, K. Z., Garnavich, P. M., Kaluzny, J., Pych, W., & Thompson, I. 1999, *ApJ*, 522, L39
 Stanek, K. Z. et al. 2007, *Acta Astronomica*, in press, (astro-ph/0604113)
 Tavani, M. 1998, *ApJ*, 497, L21
 Thomas, B. C., Jackman, C. H., Melott, A. L., Laird, C. M., Stolarski, R. S., Gehrels, N., Cannizzo, J. K., & Hogan, D. P. 2005, *ApJ*, 622, L153
 Totani, T. 1997, *ApJ*, 486, L71
 Totani, T. 1999, *ApJ*, 511, 41
 Waxman, E., Kulkarni, S. R., & Frail, D. A. 1998, *ApJ*, 497, 288
 Wick, S. D., Dermer, C. D., & Atoyan, A. 2004, *Astropart. Phys.*, 21, 125
 Wijers, R. A. M. J., Bloom, J. S., Bagla, J. S., & Natarajan, P. 1998, *MNRAS*, 294, L13
 Yamazaki, R., Yonetoku, D., & Nakamura, T. 2003, *ApJ*, 594, L79
 Zhang, B. 2006, *Nature*, 444, 1010
 Zhang, B., Dai, X., Lloyd-Ronning, N. M., & Mészáros, P. 2004, *ApJ*, 601, L119